WILEY-VCH

Boosting oxygen evolution reaction by creating both metal ion and lattice-oxygen active sites in a complex oxide

Yinlong Zhu, Hassan A. Tahini, Zhiwei Hu, Zhi-Gang Chen, Wei Zhou, Alexander C. Komarek, Qian Lin, Hong-Ji Jin, Chien-Te Chen, Yijun Zhong, M. T. Fernández-Díaz, Sean C. Smith, Huanting Wang, Meilin Liu, Zongping Shao**

Dr. Y. Zhu, Dr. Q. Lin, Prof. W. Zhou, Prof. Z. Shao
Jiangsu National Synergetic Innovation Center for Advanced Materials (SICAM), State Key Laboratory of Materials-Oriented Chemical Engineering, College of Chemical Engineering, Nanjing Tech University, No. 5 Xin Mofan Road, Nanjing 210009, P.R. China
Email: shaozp@njtech.edu.cn

Dr. H. A. Tahini, Prof. S. C. Smith
Department of Applied Mathematics, Research School of Physics and Engineering, Australian National University, Canberra 2601, Australia

Dr. Z. Hu, Dr. A. C. Komarek
Max Planck Institute for Chemical Physics of Solids, Nothnitzer Strasse 40, Dresden 01187, Germany

Prof. Z. Chen
Centre for Future Materials, University of Southern Queensland, Springfield, Queensland 4300, Australia

Prof. Z. Chen
Materials Engineering, The University of Queensland, Brisbane, Queensland 4072, Australia

Dr. H.-J. Jin, Dr. C.-T. Chen
National Synchrotron Radiation Research Center, 101 Hsin-Ann Road, Hsinchu 30076, Taiwan

Y. Zhong, Prof. Z. Shao
Department of Chemical Engineering, Curtin University, Perth, Western Australia 6845, Australia

Dr. M.T. Fernández-Díaz
Institut Laue-Langevin (ILL), 71 avenue des Martyrs, F-38042 Grenoble Cedex 9, France

Dr. Y. Zhu, Prof. H. Wang
Department of Chemical Engineering, Monash University, Clayton, Victoria 3800, Australia

Prof. M. Liu
Center for Innovative Fuel Cell and Battery Technologies, School of Materials Science and Engineering, Georgia Institute of Technology, Atlanta, GA 30332-0245 , USA

Keywords: complex oxide, coordination environment, dual active sites, honeycomb-like structure, oxygen evolution reaction

Developing efficient and low-cost electrocatalysts for oxygen evolution reaction (OER) is of paramount importance to many chemical and energy transformation technologies. The diversity and flexibility of metal oxides offer numerous degrees of freedom for enhancing catalytic activity by tailoring their physicochemical properties, but the active site of current metal oxides for OER is still limited to either metal ion or lattice-oxygen. Here we report a new complex oxide with unique hexagonal structure consisting of one honeycomb-like network, $Ba_4Sr_4(Co_{0.8}Fe_{0.2})_4O_{15}$ (hex-BSCF), demonstrating ultrahigh OER activity because both the tetrahedral Co ions and the octahedral oxygen ions on the surface are active, as conformed by combined X-ray absorption spectroscopy analysis and theoretical calculations. The bulk hex-BSCF material synthesized by the facile and scalable sol-gel method achieves 10 mA cm^{-2} at a low overpotential of only 340 mV (and small Tafel slope of 47 mV dec^{-1}) in 0.1 M KOH, surpassing most metal oxides ever reported for OER, while maintaining excellent durability. This study opens up a new avenue to dramatically enhancing catalytic activity of metal oxides for other applications through rational design of structures with multiple active sites.

Oxygen evolution reaction (OER) plays a crucial role in many electrochemical energy storage and conversion technologies such as solar/electricity-driven water splitting, rechargeable metal-air batteries, and regenerative fuel cells.[1,2] However, the OER has become a bottleneck in these electrochemical systems because of the intrinsic sluggish kinetics that involves a multistep proton-coupled electron transfer process.[2,3] A lower overpotential to reach a desirable current density is highly demanded, thus necessitating efficient electrocatalysts to expedite the reaction rate. At present, precious metal oxides (i.e., IrO_2 and RuO_2) are identified as the benchmark OER electrocatalysts with reasonably high activity, but the high cost, scarcity, and insufficient durability have seriously hindered their widespread use in practical devices.[3] Therefore, it is highly desirable to develop alternative OER electrocatalysts with high activity and robust durability derived from low-cost and earth-abundant elements.

During the past decade, non-precious transition metal oxides in various structural forms, such as spinels and perovskites, have emerged as promising candidates for OER catalysts because of their robustness, abundance, accessibility, and environmental friendliness under the environmental atmosphere.[2-5] The interplay of charge, spin, orbital and coordination degrees of freedom of 3*d* transition metal ions in metal oxides provides the flexibility of the electronic and crystal structures to meet the desirable conditions or parameters for highly active catalysts.[2-4] For spinel Co_3O_4 composed of 1/3 Co^{2+} in the tetrahedral (Td) sites (Co^{2+}_{Td}) and 2/3 Co^{3+} in the octahedral (Oh) sites (Co^{3+}_{Oh}), only the Co^{2+}_{Td} are active for OER.[6] Different from the spinel oxide, the transition metal ions in a perovskite oxide (ABO_3, where A are alkaline-earth or rare-earth metals and B are transition metals) are exclusively located at the octahedral sites and widely regarded as OER active. To date, on the basis of systematic experiments and theoretical calculations, many descriptors relevant to the bulk electronic structure of perovskites have been correlated to the OER activity determined from experiments, including e_g orbital occupancy,[7] O 2*p*-band center relative to Fermi level,[8] *d*

electron number,[9] and charge-transfer energy.[10] For example, one pioneering study conducted by Suntivich et al. proposed a dependable descriptor of the e_g occupancy of the first-row transition metal ions for OER activity; $Ba_{0.5}Sr_{0.5}Co_{0.8}Fe_{0.2}O_{3-\delta}$ (BSCF) perovskite with an optimal $e_g \approx 1.2$ displays a landmark intrinsic OER activity, about one order of magnitude higher than the state-of-the-art IrO_2 catalyst,[7] but the deteriorated long-term operational stability resulted from surface amorphization during OER process remains a serious challenge.[11]

In addition to the simple perovskite oxides, some complex oxides with special crystal structures or multiple metal coordination environments have been recently reported as promising OER catalysts with higher activity than that of simple perovskite counterparts, including pyrochlores,[12,13] double perovskites,[14,15] triple perovskites,[16] quadruple perovskites,[17,18] Ruddlesden-Popper oxides,[19] and transition metal phosphates.[20] A wide variety of structures for complex oxides can bring about some unique geometrical, electronic and conductive properties, consequently enhancing their electroctalytic activities. Despite these efforts, the adoption of noble metals (e.g., Ru/Ir for pyrochlores and double perovskites[12-15]) and harsh synthesis method (e.g., ultra-high-pressure for quadruple perovskites[17,18]) in some cases are difficult for cost-effective and large-scale manufacture in practical applications. Thus, a facile and economical route for catalyst preparation (without complicated process) is also highly desirable. Moreover, by combining powerful characterization techniques (i.e., *in-situ* isotope labelling mass spectrometry) with density functional theory (DFT) calculations, a new OER mechanism concerning lattice-oxygen activation in some highly covalent oxides was recently proposed,[21] which are fundamentally different from the conventional mechanism on surface metal sites. This new insight opens new opportunities for designing oxide-based catalysts with simultaneous metal ion and oxygen ion sites for OER catalysis; simultaneous contributions from more than one type of active sites may contribute to enhanced catalytic activity. However, the concept of making

full use of both surface metal ions and lattice-oxygen ions in oxides at the same time for OER is yet to be realized.

Motivated by the above thoughts, here we report a new class of metal oxide prepared by a facile sol-gel method, $Ba_4Sr_4(Co_{0.8}Fe_{0.2})_4O_{15}$ (hex-BSCF), as a highly active and durable OER electrocatalyst in alkaline solution. This complex oxide crystallizes in a hexagonal structure with Co/Fe ions occupying two distinctly different crystallographic sites: tetrahedral and octahedral sites. The hex-BSCF shows a remarkable OER activity with an extremely low overpotential of 340 mV at 10 mA cm^{-2} and a very small Tafel slope of 47 mV dec^{-1} in 0.1 M KOH, which is superior to those of the benchmark noble-metal RuO_2 and well-known BSCF catalysts. First-principles calculations suggest that both surface metal ions and lattice-oxygen ions are active, resulting in exceptionally high catalytic activity. The activity of the ions at these sites originates from the favorable electronic structure of Co ions at T_d and O_h sites tuned by Fe substitution, as confirmed by X-ray absorption spectroscopy (XAS). Specifically, the high spin Co^{3+}/Co^{4+} ions in the tetrahedral site (HS $Co^{3+/4+}{}_{Td}$) give rise to the conventional OER mechanism on surface metal sites, while lattice-oxygen participation mechanism mediated by O 2*p* ligand holes is triggered through the strong covalent bonds between octahedrally coordinated intermediate spin Co^{4+} ion (IS $Co^{4+}{}_{Oh}$) and oxygen ion. Our findings provide a new framework for developing highly efficient electrocatalysts via the possible dual-center catalytic pathway.

The new family of complex oxides with the chemical formula of $A_8B_4O_{15}$ (A=Ba,Sr; B=Co,Fe) generally crystallizes in a hexagonal structure where Co/Fe ions are located at the tetrahedral and octahedral sites (oxygen coordination number of 4 and 6, respectively) (**Figure 1**a). One $(Co/Fe)O_6$ octahedron and three $(Co/Fe)O_4$ tetrahedra are connected by shared oxygen atoms to form $(Co/Fe)_4O_{15}$ clusters, which are packed together into a honeycomb-like network (Figure 1b). We started with the density functional theory (DFT) calculations to guide the rational design of complex oxides with such structural motifs. The

partial density of states (DOS) calculations of $Sr_8Co_4O_{15}$, $Ba_8Co_4O_{15}$, $Ba_4Sr_4Co_4O_{15}$ (denoted as hex-BSC) and Fe-substituted $Ba_4Sr_4(Co_{0.8}Fe_{0.2})_4O_{15}$ (denoted as hex-BSCF) were performed for the proof-of-concept study (Figure S1). The projected DOS presents a metallic behavior of hex-BSCF with predominantly Co, Fe, and O states crossing the Fermi level, which is beneficial to the electron transfer during the OER electrocatalysis.[22] The O 2*p*-band center was also calculated considering that it has been regarded as an effective descriptor for OER catalytic activity of oxides as demonstrated previously.[8] As seen from Figure 1c, the O 2*p*-band center of hex-BSC is much higher relative to the pristine $Sr_8Co_4O_{15}$ and $Ba_8Co_4O_{15}$. The O 2*p*-band center could be further upshifted upon the low level Fe substitution, implying that hex-BSCF would boost the OER. In light of these findings of DFT calculation, the hex-BSCF is expected to be highly active for OER and accordingly we sought to prepare the hex-BSCF oxide. The hex-BSC and hex-BSCF oxide were successfully synthesized via a facile and scalable sol-gel method, and the crystal structure was initially verified by X-ray diffraction (XRD) (Figure S2). Rietveld refinement of the XRD pattern reveals that the hex-BSCF adopts a hexagonal structure with a space group of $P6_3mc$ (Figure 1d). To obtain more precise structural information, specifically the oxygen content in the hex-BSCF, neutron powder diffraction (NPD) measurement was also performed. Rietveld refinement of the NPD pattern demonstrates the hexagonal structure and almost oxygen stoichiometry of hex-BSCF (Figure 1e and Table S1). The crystal structure of hex-BSCF was further confirmed by two selected-area electron-diffraction (SAED) patterns along the $[1\bar{1}00]$ and [0001] zone axes (Figure 1f & g) and the corresponding high-resolution transmission electron microscopy (HRTEM) images (Fig. 1h & i). In addition, micrometer-sized particles were observed in scanning electron microscopy (SEM) images, suggesting the bulk nature of the as-synthesized hex-BSC and hex-BSCF oxides (Figure S3). The unique structural motif in hex-BSCF plays a significant role in improving the OER activity, as to be discussed below.

The OER performance of hex-BSC and hex-BSCF catalysts was assessed using a typical rotating disk electrode (RDE) technique.[7,23] For direct comparison, the OER performance of the well-known BSCF perovskite and benckmark RuO_2 catalyst was measured under the same conditions (See Figure S4 and Figure S5 for detailed information). All electrode potentials reported in this study were calibrated with respect to reversible hydrogen electrode (RHE, Figure S6) and *iR*-corrected to eliminate the ohmic potential drop across the electrolyte. **Figure 2**a shows the capacitance- and ohmic resistance-corrected polarization curves obtained from cycle voltammetry (CV, Figure S7) of hex-BSC, hex-BSCF, BSCF, and RuO_2 catalysts in O_2-saturated 0.1 M KOH solution. The overpotential (η) for the hex-BSCF catalyst at each current density is lower than that for the hex-BSC, BSCF and even the benckmark RuO_2, suggesting the highest OER electrode activity among the catalysts studied. Remarkably, the η for hex-BSCF is extremely small (only ~340 mV) for achieving 10 mA cm^{-2} (which is a metric related to solar fuel synthesis[24]), much lower than that for the hex-BSC (398 mV), BSCF (505 mV), and RuO_2 (426 mV) catalysts. As seen from the Tafel plots shown in Figure 2b, the Tafel slope for hex-BSCF (47 mV dec^{-1}) is smaller than that for hex-BSC (59 mV dec^{-1}), BSCF (77 mV dec^{-1}), and RuO_2 (95 mV dec^{-1}) catalysts, implying faster OER rate. The Tafel plots derived from capacitance-corrected CV curves are similar to the plots obtained from the steady-state measurements (Figure S8). Additionally, we also calculated the mass activity (MA, normalized to the oxide mass loading) and specific activity (SA, normalized to the oxide surface area as estimated from BET measurements in Table S2 or the electrochemical surface area as estimated from double-layer capacitance in Figure S9). Considering that MA is important for practical applications and SA reflects the catalyst's intrinsic activity,[7,25] it would be meaningful to compare the MA and SA among the catalysts studied. As seen from Figure 2c, the MA of hex-BSCF at η=0.35 V is ~7.4, ~ 42.6, and ~4.2 times higher than that of hex-BSC, BSCF, and RuO_2, respectively. Further, the SA for the hex-BSCF is also significantly higher than those for other catalysts studied, normalized either

by the BET surface area or electrochemical surface area (ECSA) (Figure 2c and Figure S10). For example, the SA for the hex-BSCF is ~1.91 mA cm^{-2}_{oxide}, which is ~15.0 and ~16.5 times higher than that for the hex-BSC and RuO_2, respectively. It is still ~6.1 higher than that for BSCF perovskite, well-known for its superior intrinsic OER activity. Also, it is noted that the substitution of Co by Fe in $Ba_4Sr_4(Co_{1-x}Fe_x)_4O_{15}$ ($0 \leq x \leq 1$) yields a volcano-like catalytic trend, with 20% Fe substitution (i.e., hex-BSCF) being the highest (Figure S11). The excellent catalytic activity for OER demonstrated by hex-BSCF is superior to those of any state-of-the-art oxide-based catalysts ever reported (Figure 2d and Table S3).

In addition to the activity, the stability is also a critical criterion to evaluate the practical value of an electrocatalyst. The continuous CV scans for hex-BSCF and other Fe-substituted compositions in $Ba_4Sr_4(Co_{1-x}Fe_x)_4O_{15}$ (e.g., x=0.1 and 0.5) generates negligible changes in the CV data or the capacitive current, indicating good stability during OER (Figure 2e and Figure S12). In contrast, considerable changes in CV curves were observed under the same testing conditions for BSCF, where the surface becomes amorphous.[11] The good durability of the hex-BSCF was further demonstrated by chronopotentiometry (CP) test. The overpotential for hex-BSCF remains almost unchanged during 10 h test, whereas the overpotential for hex-BSC and RuO_2 increases distinctly (Figure 2f). Further evidence to support the stability of hex-BSCF during OER was from TEM, XAS, XRD and CV analysis. Neither surface amorphization in TEM images nor variation in XRD and XAS peaks was observed for hex-BSCF catalyst before and after 50-cycle CV scans (Figure 2g & h**,** Figure S13 and Figure S14), demonstrating the hex-BSCF is stable without structure reconstruction under OER. An amorphous layer was formed for Fe-free hex-BSC after continuous CV measurements (Figure S15), implying that some substitution of Co by Fe may stabilize the crystal structure, as also reported elsewhere.[26-28] Besides, the change in pseudocapacitive and OER currents during CV cycling has been regarded as a good indicator of surface structural variation of catalysts.[11,29-31] Both the capacitive and OER current of BSCF continued to increase during

further cycling (Figure S12B), suggesting an activation process with surface structure reconstruction, which is consistent with previous reports[11]. On contrary, neither noticeable change in pseudocapacitive current nor in OER current was observed during the first 50 cycles for hex-BSCF (Figure 2E). The good structure stability of hex-BSCF under OER may be originated mainly from its unique hexagonal crystal structure (combined tetrahedral and octahedral coordinations) and high valence state of metal ions (as to be confirmed below).

In order to demonstrate the applicability to water splitting, we constructed a two-electrode electrolyzer using carbon fiber paper (CFP) loaded with hex-BSCF OER catalyst as the anode and with the benchmark Pt catalyst (active for hydrogen evolution reaction) as the cathode (Figure S16). At a water-splitting current density of 10 mA cm^{-2}, the cell voltage was only ~1.56 V, much lower than that for the cells with RuO_2 (+)//Pt(-) and BSCF(+)//Pt(-) electrode couples. Moreover, the cell with the hex-BSCF anode also showed better durability than those with the RuO_2 and BSCF anodes.

To gain some insight into the origin of the outstanding OER performance of hex-BSCF, we characterized the electronic structures of the catalysts studied, using soft X-ray absorption spectroscopy (XAS) with the surface-sensitive total electron yield (TEY) mode (~5 nm), such as the spin, orbital, valence state, and local coordination of the ions.[4,8,12-14,32-35] **Figure 3**a shows the Co L_3-edge XAS spectra of the hex-BSC, hex-BSCF, and several reference materials with different valence states of Co, including CoO (divalent), $YBaCo_4O_7$ (trivalent, tetrahedral coordination),[36] and $SrCoO_3$ (tetravalent).[37] The Co $L_{2,3}$-edges are highly sensitive to Co ion's valence states and spin states. The edge peak shifts to higher energy from CoO to $YBaCo_4O_7$, hex-BSCF, hex-BSC, and further $SrCoO_3$, suggesting the coexistence of Co^{3+} and Co^{4+} in hex-BSCF and hex-BSC as well as slightly lower Co valence state of hex-BSCF relative to hex-BSC. It is previously reported that the Co^{3+}/Co^{4+} ions located at tetrahedral (Td) sites for hex-BSC exhibit the high-spin (HS) state and Co^{4+} ions located at octahedral (Oh) sites show the intermediate-spin (IS) state.[38] To extract the accurate valence

and spin state of Co ions in hex-BSC and hex-BSCF, we simulated the experimental Co $L_{2,3}$-edge XAS spectral by superposing the spectra of relevant references: HS Co^{3+}_{Td} for $YBaCo_4O_7$,[36] HS Co^{4+}_{Td} for Ba_2CoO_4,[39] and IS Co^{4+}_{Oh} for $SrCoO_3$.[37] The simulated sum curves in Figure 3b and Figure 3c well reproduce the experimental spectra, demonstrating goodness of fit. The average valence state of Co ions for hex-BSC was calculated to be +3.5 based on the fitted result of 50% HS Co^{3+}_{Td}, 25% HS Co^{4+}_{Td}, and 25% IS Co^{4+}_{Oh} (Figure 3b), corresponding to the 3:1 tetrahedral/octahedral site ratio for the Co ions. For 20% substitution of Co by Fe ion, the average valence state of Co ions in hex-BSCF decreases slightly to +3.4, resulted from more occupation of Co^{3+}_{Td} (Figure 3c). Such results suggest that in hex-BSCF, Fe ions preferentially occupies the octahedral sites (Fe^{4+}_{Oh}) and confines Co ions to the tetrahedral site (Co^{3+}_{Td}), as also verified by the Fe-sensitive Mössbauer spectroscopy (Figure S17 and Table S4). The Fe L_3-edge XAS spectra further confirms the mixture of Fe^{3+}/Fe^{4+} in hex-BSCF (Figure S18). To explore the degree of covalency of TM 3*d* orbitals and O 2*p* states, soft XAS measurement in TEY mode at the O-*K* edge was performed (Figure 3d). As seen from Figure 3d (bottom), the pre-edge peak shifts to lower energies and the spectral weight becomes higher as the Co valence increase from CoO to $YBaCo_4O_7$ and further to $SrCoO_3/Ba_2CoO_4$, suggesting the increased Co-O covalency.[8,40] The low energy O-*K* pre-edge peak located at ~527.7 eV were observed for hex-BSC and hex-BSCF, further indicating the existence of high-valence Co^{4+}/Fe^{4+} ions with strong metal-oxygen covalency. To sum up, the above XAS analysis demonstrates that the Co ions in the tetrahedral sites of hex-BSCF are HS $Co^{3+/4+}$ while the octahedral Co ions are IS Co^{4+}. Figure 3e schematically depicts the electron configuration of e/t_2 orbitals of tetrahedrally-coordinated HS $Co^{3+/4+}$ and octahedrally-coordinated IS Co^{4+} in the hex-BSCF.

Previous studies have shown that some metal ions in the tetrahedral coordination are active for catalyzing OER, such as Co^{2+}_{Td} in Co_3O_4,[6] $Na_2CoP_2O_7$,[20] β_{II} Li_2CoSiO_4[41] and Mn^{3+}_{Td} in α-Mn_3O_4.[42] In this regard, the $Co^{3+/4+}_{Td}$ ions in hex-BSCF are anticipated to act as

OER active sites, which is consistent with our DFT calculations (presented below). The involvement of lattice-oxygen mediated by oxygen holes in OER catalysis was also proposed recently and great covalency of metal-oxygen bonds is critical to trigger this mechanism.[21] The O 2*p*-band center and the charge transfer energy are two important descriptors for catalyst design and both are directly related to the covalence state of metal ion.[4,8,10,21] Currently it has been reported that the covalence increases with increasing the oxidation state of metal ions,[21,37] which is also reflected by the Co-$L_{2,3}$ and the O-*K* XAS in this study (Figure 3a-d). By increasing the valence of the metal ions by one, the value of charge transfer energy is reduced by about 3-4 eV,[43] and the O 2*p* character moves upwards and even cross E_F for Co^{4+} (Figure 3f).[34] In addition, the covalent degree of O 2*p* states and Co 3*d* orbitals is also related to the local coordination environment.[41] The high lying unoccupied e_g orbitals for Co^{4+} ion with Oh symmetry has a relatively strong covalence than the t_2 orbitals for Co^{4+} ion with Td symmetry (Figure 3e), leading to more negative charge transfer energy and more O 2*p* band above E_F (i.e., ligand hole).[44] Therefore, the $Co^{4+}{}_{Oh}$ with a dominant $3d^6\underline{L}$ configuration ($\underline{L}$ represents an O 2*p* ligand hole) can trigger lattice-oxygen oxidation in view of its great covalency of metal-oxygen bonds.[21] When the O 2*p* states at the Fermi level lie above the redox energy of the H_2O/O_2 couple, the oxidation of lattice oxygen becomes thermodynamically favorable (Figure 3f). However, the O 2*p* hole in $Co^{4+}{}_{Oh}$ triggering lattice oxygen involvement is prone to be unstable under oxidizing conditions,[14] as also reflected by the poor OER stability for hex-BSC with high level of holes. Robust structure stability during OER operation for hex-BSCF implies that the Fe substitution could help to stabilize the $Co^{4+}{}_{Oh}$. In addition to the role of stabilizing the structure and $Co^{4+}{}_{Oh,}$ low level substitution of Co by Fe also results in (i) increased electrical conductivity as reflected form the calculated DOS; (ii) a geometrical confinement of Co ions in the tetrahedral sites; (iii) an average Co valence state of +3.4, which is similar to the optimal value in $SrCoO_{2.7}$;[45] (iv) a favorable O 2*p*-band center correlating with high intrinsic activity (Figure S19). Due to the unique

combination of tetrahedral and octahedral coordinations of $(Co, Fe)^{4+}/(Co, Fe)^{3+}$ ions in the hexagonal structure, the hex-BSCF generates a suitable O 2*p*-band center (~1.57 eV) relative to the Fermi level. Further moving O 2*p*-band center closer to the Fermi level (e.g., for BSCF) or increasing the oxidation state of Co ions (e.g., for hex-BSC) will not lead to the increase in the OER activity but decrease the oxide stability during OER. Too high oxidation state of metal ion will create the unstable O 2*p* hole at E_F and the crystal structure becomes unstable under electrochemical reaction.[46] Thus, the observed superior OER activity and durability of the hex-BSCF catalyst are attributed the geometric and electronic modifications of Co ions tuned by Fe substitution.

To further understand the reaction mechanisms and possible active sites of hex-BSCF, we resorted to DFT calculations. Two different OER mechanisms were considered: the conventional mechanism on metal sites in accordance with the Nørskov's method[47,48] (**Figure 4**a) and recently proposed lattice-oxygen participation mechanism derived from the work by Shao-Horn et al.[21] (Figure 4d). The conventional mechanism on metal-ion centre involves four concerted proton-electron transfer steps with a series of intermediates, HO^*, O^*, and HOO^* (* represents the surface metal sites),[47] while the lattice oxygen-participated mechanism involves a lattice-oxygen oxidation and non-concerted proton-electron transfer.[21] Figure 4b & c and Figure 4e & f show the free energy diagrams under different potential U of hex-BSCF on tetrahedral and octahedral Co and O sites via above two OER mechanisms. The insets are as-built surface structure models of hex-BSCF with adsorbates, which are also displayed in Figure S20 in order to be more visible. As can be seen, the theoretical overpotential (η) of tetrahedral Co (Co_{Td}) site was calculated to be 0.37 V, which is significantly lower than that (0.97 V) of octahedral Co (Co_{Oh}) site, suggesting that the tetrahedral Co site is highly active for OER. Such theoretical η for Co_{Td} in hex-BSCF is even lower that of active G-FeCoW (0.40 V),[32] $Na_2CoP_2O_7$ (0.42 V)[20] and β-CoOOH (0.48 V).[49] The high activity of Co_{Td} site in hex-BSCF possibly associates with the unique electronic

structure as revealed by aforementioned XAS study. Meanwhile, the octahedral O (O_{Oh}) site generates a lower η of 0.42 V than the tetrahedral O site ($O_{Td,}$ 0.89 V), implying the activation of octahedral lattice oxygen for OER catalysis. The high activity of O_{Oh} site originates from the high metal valence state (e.g., Co^{4+}) with strong metal-oxygen covalency.[21] Besides, the free energy on Fe sites with tetrahedral and octahedral coordination was also calculated. It was found that both Fe sites produce high theoretical overpotentials (Figure S21), excluding the possibility that the Fe ions in hex-BSCF are active sites. Therefore, these theoretical calculations suggest the coexistence of dual active sites for OER (i.e., tetrahedral Co and octahedral O sites), resulting in outstanding OER behavior of hex-BSCF, as demonstrated by above experimental results.

In summary, we have demonstrated that a hexagonal oxide $Ba_4Sr_4(Co_{0.8}Fe_{0.2})_4O_{15}$ (hex-BSCF), featured in the unique tetrahedral and octahedral Co/Fe coordinations, exhibits extraordinary activity for OER. When tested in an electrochemical cell, the electrode with the hex-BSCF catalyst displayed a low overpotential of only ~340 mV at a current density of 10 mA cm^{-2} (and a small Tafel slope of 47 mV dec^{-1}) in 0.1 M KOH solution, demonstrating the highest OER activity among metal oxides ever reported. Moreover, the hex-BSCF catalyst displays much higher OER activity (including both intrinsic and mass activity) than the state-of-the-art RuO_2 and $Ba_{0.5}Sr_{0.5}Co_{0.8}Fe_{0.2}O_{3-\delta}$ catalysts while maintaining superior durability under OER conditions. Combined XAS and DFT studies reveal that both tetrahedral Co ions and octahedral O ions on the surface are active sites, benefited from favorable local coordination environment and electronic structure, resulting in exceptionally high OER activity of hex-BSCF catalyst, while the enhanced durability is attributed to proper iron substitution. Our proof-of-concept study not only creates a highly active and durable OER electrocatalyst, but also opens up a new avenue to the development of advanced electrocatalysts for other applications via unique structural design with multiple active sites.

Supporting Information

Supporting Information is available from the Wiley Online Library or from the author.

Acknowledgements

This work was financially supported by the Defense industrial technology development program (JCKY2018605B006), National Nature Science Foundation of China (Grant No. 21576135), the Jiangsu Nature Science Foundation for Distinguished Young Scholars (Grant No. BK20170043), and the Australian Research Council (Discovery Early Career Researcher Award No. DE190100005). We acknowledge support from the Max Planck-POSTECH-Hsinchu Center for Complex Phase Materials and valuable suggestion of Prof. L.H. Tjneg.

References

[1] S. Z. W. Seh, J. Kibsgaard, C. F. Dickens, Ib Chorkendorff, J. K. Nørskov, T. F. Jaramillo, *Science* **2017**, *355*, eaad4998.

[2] D. Chen, C. Chen, Z. M. Baiyee, Z. Shao, F. Ciucci, *Chem. Rev.* **2015**, *115*, 9869.

[3] F. Song, L. Bai, A. Moysiadou, S. Lee, C. Hu, L. Liardet, X. Hu, *J. Am. Chem. Soc.* **2018**, *140*, 7748.

[4] J. Hwang, R. R. Rao, L. Giordano, Y. Katayama, Y. Yu, Y. Shao-Horn, Perovskites in catalysis and electrocatalysis. *Science* **2017**, *358*, 751.

[5] Y. Zhu, H. A. Tahini, Z. Hu, J. Dai, Y. Chen, H. Sun, W. Zhou, M. Liu, S. C. Smith, H. Wang, Z. Shao, *Nat. Commun.* **2019**, *10*, 149.

[6] H. Y. Wang, S. F. Hung, H. Y. Chen, T. S. Chan, H. M. Chen, B. Liu, *J. Am. Chem. Soc.* **2015**, *138*, 36.

[7] J. Suntivich, K. J. May, H. A. Gasteiger, J. B. Goodenough, Y. Shao-Horn, *Science* **2011**, *334*, 1383.

[8] A. Grimaud, K. J. May, C. E. Carlton, Y. L. Lee, M. Risch, W. T. Hong, J. Zhou, Y. Shao-Horn, *Nat. Commun.* **2013**, *4*, 2439.

[9] F. Calle-Vallejo, N. G. lnoglu, H. Y. Su, J. I. Martínez, I. C. Man, M. T. M. Koper, J. R. Kitchin, J. Rossmeisl, *Chem. Sci.* **2013**, *4*, 1245.

[10] W. T. Hong, K. A. Stoerzinger, Y. L. Lee, L. Giordano, A. Grimaud, A. M. Johnson, J. Hwang, E. J. Crumlin, W. Yang, Y. Shao-Horn, *Energy Environ. Sci.* **2017**, *10*, 2190.

[11] K. J. May, C. E. Carlton, K. A. Stoerzinger, M. Risch, J. Suntivich, Y. L. Lee, A. Grimaud, Y. Shao-Horn, *J. Phys. Chem. Lett.* **2012**, *3*, 3264.

[12] J. Park, M. Risch, G. Nam, M. Park, T. J. Shin, S. Park, M. G. Kim, Y. Shao-Horn, J. Cho, *Energy Environ. Sci.* **2017**, *10*, 129.

[13] K. Kim, P. C. Shih, Y. Qin, Z. Al-Bardan, C. J. Sun, H. Yang, *Angew. Chem. Int. Ed.* **2018**, *130*, 14073.

[14] A. Grimaud, A. Demortière, M. Saubanère, W. Dachraoui, M. Duchamp, M. L. Doublet, J. M. Tarascon, *Nat. Energy* **2017**, *2*, 16189.

[15] O. Diaz-Morales, S. Raaijman, R. Kortlever, P. J. Kooyman, T. Wezendonk, J. Gascon, W. T. Fu, M. T. M. Koper, *Nat. Commun.* **2016**, *7*, 12363.

[16] N. I. Kim, Y. J. Sa, T. S. Yoo, S. R. Choi, R. A. Afzal, T. Choi, Y. S. Seo, K. S. Lee, J. Y. Hwang, W. S. Choi, S. H. Joo, J. Y. Park, *Sci. Adv.* **2018**, *4*, eaap9360.

[17] S. Yagi, I. Yamada, H. Tsukasaki, A. Seno, M. Murakami, H. Fujii, H. Chen, N. Umezawa, H. Abe, N. Nishiyama, S. Mori, *Nat. Commun.* **2015**, *6*, 8249.

[18] I. Yamada, H. Fujii, A. Takamatsu, H. Ikeno, K. Wada, H. Tsukasaki, S. Kawaguchi, S. Mori, S. Yagi, *Adv. Mater.* **2017**, *29*, 1603004.

[19] R. P. Forslund, W. G. Hardin, X. Rong, A. M. Abakumov, D. Filimonov, C. T. Alexander, J. T. Mefford, H. lyer, A. M. Kolpak, K. P. Johnston, K. J. Stevenson, *Nat. Commun.* **2018**, *9*, 3150.

[20] H. Kim, J. Park, I. Park, K. Jin, S. E. Jerng, S. H. Kim, K. T. Nam, K. Kang, *Nat. Commun.* **2015**, *6*, 8253.

[21] A. Grimaud, O. Diaz-Morales, B. Han, W. T. Hong, Y. L. Lee, L. Giordano, K. A. Stoerzinger, M. T. M. Koper, Y. Shao-Horn, *Nat. Chem.* **2017**, *9*, 457.

[22] T. Zheng, W. Sang, Z. He, Q. Wei, B. Chen, H. Li, C. Cao, R. Huang, X. Yan, B. Pan, S. Zhou, J. Zeng, *Nano Lett.* **2017**, *17*, 7968.

[23] J. Suntivich, H. A. Gasteiger, N. Yabuuchi, Y. Shao-Horn, *J. Electrochem. Soc.* **2010**, *157*, B1263.

[24] C. C. McCrory, S. Jung, J. C. Peters, T. F. Jaramillo, *J. Am. Chem. Soc.* **2013**, *135*, 16977.

[25] B. Zhao, L. Zhang, D. Zheng, S. Yoo, Y. Ding, D. Chen, Y. Chen, Q. Zhang, B. Doyle, X. Xiong, M. Liu, *Nat. Commun.* **2017**, *8*, 14586.

[26] Y. Zhu, W. Zhou, Y. Chen, J. Yu, M. Liu, Z. Shao, *Adv. Mater.* **2015**, *27*, 7150.

[27] J. Y. C. Chen, L. Dang, H. Liang, W. Bi, J. B. Gerken, S. Jin, E. E. Alp, S. S. Stahl, *J. Am. Chem. Soc.* **2015**, *137*, 15090.

[28] S. F. Hung, Y. Y. Hsu, C. J. Chang, C. S. Hsu, N. T. Suen, T. S. Chan, H. M. Chen, *Adv. Energy Mater.* **2018**, *8*, 1701686.

[29] S. W. Lee, C. Carlton, M. Risch, Y. Surendranath, S. Chen, S. Furutsuki, A. Yamada, D. G. Nocera, Y. Shao-Horn, *J. Am. Chem. Soc.* **2012**, *134*, 16959.

[30] Y. Duan, S. Sun, Y. Sun, S. Xi, X. Chi, Q. Zhang, X. Ren, J. Wang, S. J. H. Ong, Y. Du, L. Gu, A. Grimaud, Z. J. Xu, *Adv. Mater.* **2019**, *31*, 1807898.

[31] H. Jiang, Q. He, X. Li, X. Su, Y. Zhang, S. Chen, S. Zhang, G. Zhang, J. Jiang, Y. Luo, P. M. Ajayan, L. Song, *Adv. Mater.* **2019**, *31*, 1805127.

[32] B. Zhang, X. Zheng, O. Voznyy, R. Comin, M. Bajdich, M. García-Melchor, L. Han, J. Xu, M. Liu, L. Zheng, F. P. García de Arquer, C. T. Dinh, F. Fan, M. Yuan, E. Yassitepe, N. Chen, T. Regier, P. Liu, Y. Li, P. D. Luna, A. Janmohamed, H. L. Xin, H. Yang, A. Vojvodic, E. H. Sargent, *Science* **2016**, *352*, 333.

[33] T. Burnus, Z. W. Hu, H. H. Hsieh, V. L. J. Joly, P. A. Joy, M. W. Haverkort, H. Wu, A. Tanaka, H.-J. Lin, C.-T. Chen, L. H. Tjeng, *Phys. Rev. B* **2008**, *77*, 125124.

[34] T. Burnus, Z. W. Hu, H. Wu, J. C. Cezar, S. Niitaka, H. Takagi, C. F. Chang, N. B. Brookes, H.-J. Lin, L. Y. Jang, A. Tanaka, K. S. Liang, C.-T. Chen, L. H. Tjeng, *Phys. Rev. B* **2008**, *77*, 205111.

[35] J.-M. Chen, Y.-Y. Chin, M. Valldor, Z. W. Hu, J.-M. Lee, S.-C. Haw, N. Hiraoka, H. Ishii, C.-W. Pao, K.-D. Tsuei, J.-F. Lee, H.-J. Lin, L.-Y. Jang, A. Tanaka, C.-T. Chen, L. H. Tjeng, *J. Am. Chem. Soc.* **2014**, *136*, 1514.

[36] N. Hollmann, Z. Hu, M. Valldor, A. Maignan, A. Tanaka, H. H. Hsieh, H. J. Lin, C. T. Chen, L. H. Tjeng, *Phys. Rev. B* **2009**, *80*, 085111.

[37] R. H. Potze, G. A. Sawatzky, M. Abbate, *Phys. Rev. B* **1995**, *51*, 11501.

[38] V. O. Garlea, R. Jin, E. Garlea, G. Ehlers, E. Mamontov, D. B. Myers, F. Xie, R. Custelcean, *Phys. Rev. B* **2012**, *86*, 094434.

[39] R. Jin, H. Sha, P. G. Khalifah, R. E. Sykora, B. C. Sales, D. Mandrus, J. Zhang, Ba_2CoO_4: *Phys. Rev. B* **2006**, *73*, 174404.

[40] T. Mizokawa, Y. Wakisaka, T. Sudayama, C. lwai, K. Miyoshi, J. Takeuchi, H. Wadati, D. G. Hawthorn, T. Z. Regier, G. A. Sawatzky, *Phys. Rev. Lett.* **2013**, *111*, 056404.

[41] J. Yang, J. Zheng, M. Xu, Z. Zhuo, W. Yang, L. W. Wang, L. Dai, J. Lu, K. Amine, F. Pan, *ACS Catal.* **2018**, *8*, 466.

[42] Z. M. Chan, D. A. Kitchaev, J. N. Weker, C. Schnedermann, K. Lim, G. Ceder, W. Tumas, M. F. Toney, D. G. Nocera, *Proc. Natl. Acad. Sci. U. S. A.* **2018**, *115*, E5261.

[43] A. E. Bocquet, T. Mizokawa, T. Saitoh, H. Namatame, A. Fujimori, *Phys. Rev. B* **1992**, *46*, 3771.

[44] A. A. Tsirlin, M. G. Rabie, A. Efimenko, Z. Hu, R. Saez-Puche, L. H. Tjeng, *Phys. Rev. B* **2014**, *90*, 085106.

[45] H. Liu, J. Zhou, L. Zhang, Z. Hu, C. Kuo, J. Li, Y. Wang, L. H. Tjeng, T. W. Pi, A. Tanaka, L. Song, J. Q. Wang, S. Zhang, *J. Phys. Chem. C* **2017**, *121*, 16079.

[46] J. T. Mefford, X. Rong, A. M. Abakumov, W. G. Hardin, S. Dai, A. M. Kolpak, K. P. Johnston, K. J. Stevenson, *Nat. Commun.* **2016**, *7*, 11053.

[47] I. C. Man, H. Y. Su, F. Calle-Vallejo, H. A. Hansen, J. I. Martínez, N. G. Inoglu, J. Kitchin, T. F. Jaramillo, J. K. Nørskov, J. Rossmeisi, *ChemCatChem* **2011**, *3*, 1159.

[48] J. Rossmeisl, Z. W. Qu, H. Zhu, G. J. Kroes, J. K. Nørskov, *J. Electroanal. Chem.* **2017**, *607*, 83.

[49] M. Bajdich, M. García-Mota, A. Vojvodic, J. K. Nørskov, A. T. Bell, *J. Am. Chem. Soc.* **2013**, *135*, 13521.

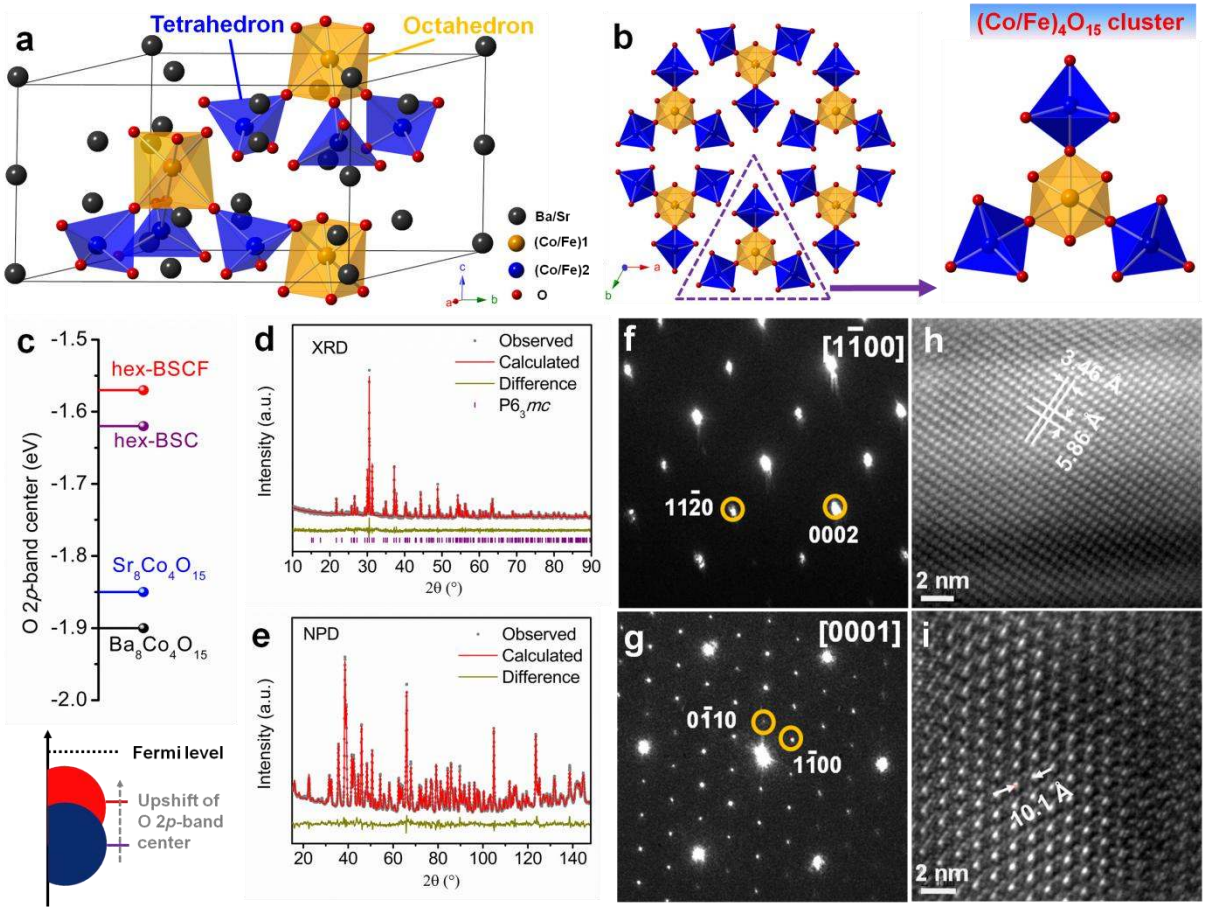

Figure 1. Structural characterization of hex-BSCF. (a) Perspective view of the crystal structure of the hex-BSCF. (b) Honeycomblike layers of Co/Fe atoms projected along the crystallographic *c* direction. (c) Calculated O 2*p*-band center relative to the Fermi level. (d) Refined XRD profile of the hex-BSCF. (e) Refined NPD profile of the hex-BSCF. Observed (gray solid circle), calculated (red solid line), differences (dark yellow line, bottom), and calculated Bragg positions (vertical purple bars) for each phase are presented. (f, g) SAED patterns and (h, i) the corresponding HRTEM images along the [1$\bar{1}$00] and [0001] zone axes for hex-BSCF.

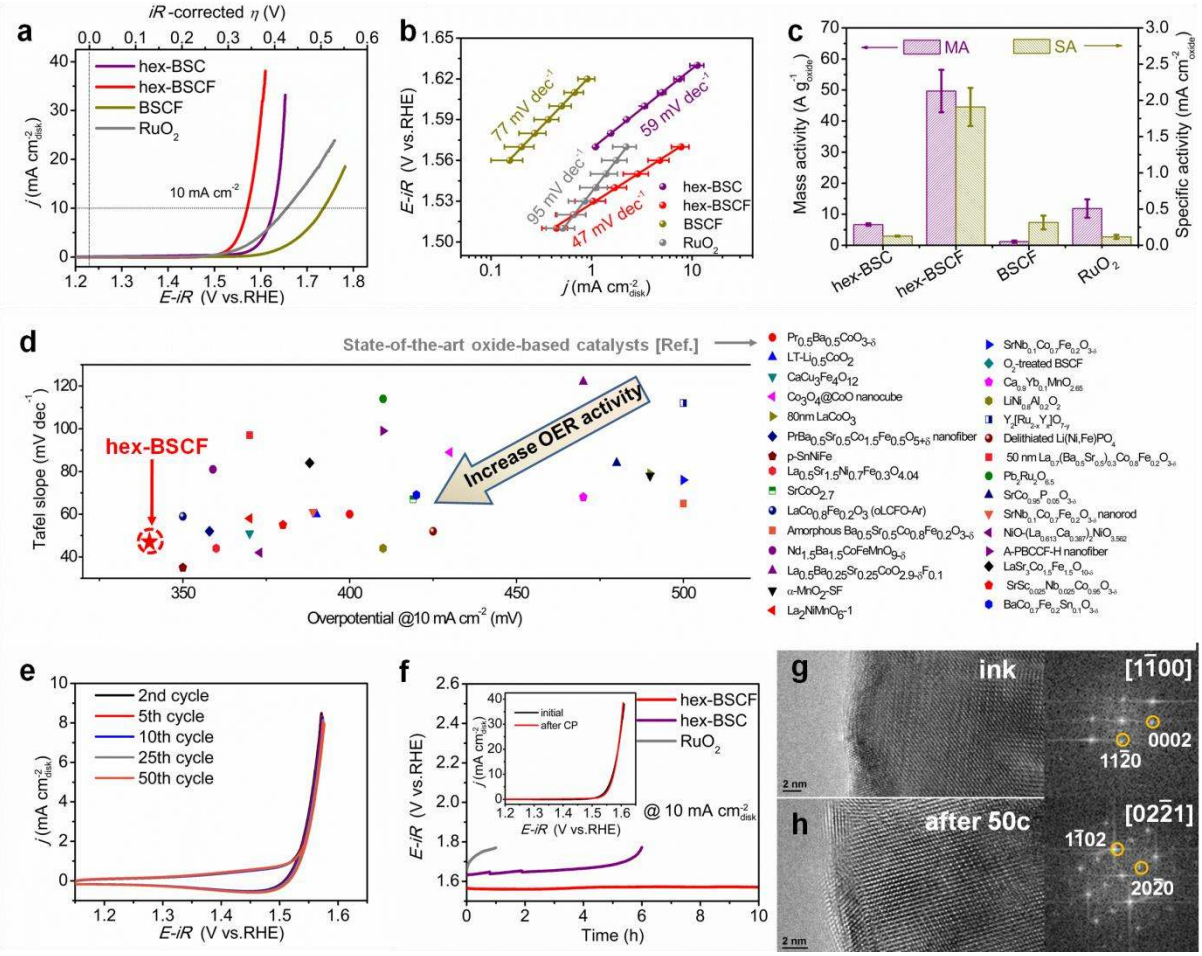

Figure 2. Electrocatalytic performance of catalysts. (a) Capacitance- and ohmic resistance-corrected polarization curves of hex-BSC, hex-BSCF, BSCF and RuO_2 catalysts in O_2-saturated 0.1 M KOH solution at a scan rate of 10 mV s^{-1}. (b) Corresponding Tafel plots derived from the data shown in a. (c) Mass activities and BET surface area-normalized specific activities of hex-BSC, hex-BSCF, BSCF, and RuO_2 catalysts at η = 0.35 V. The error bars represent standard deviations from three independent measurements. (d) OER activity comparison graph showing the Tafel slope with overpotential@10 mA cm^{-2} for hex-BSCF and reported state-of-the-art oxide-based electrocatalysts. (e) The 2nd, 5th,10th, 25th and 50th CV scans of hex-BSCF. (f) Chronopotentiometric (CP) curves of the hex-BSCF, hex-BSC, and RuO_2 catalysts at 10 mA cm^{-2}_{disk}. Inset in f is the polarization curves of the hex-BSCF before and after the CP test. HRTEM images and the corresponding FFT patterns of the hex-BSCF after (g) ink preparation process and (h) 50-cycle CV scans.

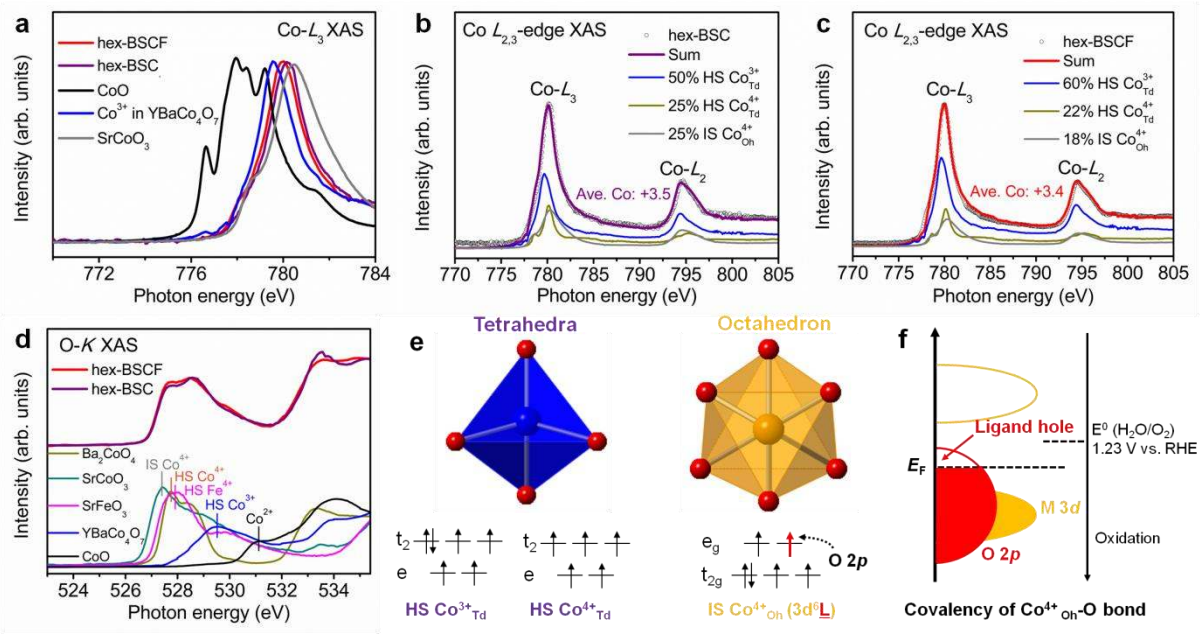

Figure 3. Surface electronic structures of the catalysts. (a) The Co-L_3 XAS spectra of hex-BSC, hex-BSCF, and several reference materials. Simulation of the Co $L_{2,3}$ XAS spectra of (b) hex-BSC and (c) hex-BSCF by superposition of the spectral information from relevant reference materials: $YBaCo_4O_7$ as HS Co^{3+}_{Td}, Ba_2CoO_4 as HS Co^{4+}_{Td}, and $SrCoO_3$ as IS $Co^{4+}_{Oh.}$ (d) The O-K XAS spectra of hex-BSC, hex-BSCF, and several reference materials. (e) The electronic structure of a Co ion at the tetrahedral and octahedral site in hex-BSCF. (f) Schematic illustration of the relationship between O 2p ligand hole and Co^{4+}_{Oh}-O covalent bond. The standard Nernstian potential position of the H_2O/O_2 redox couple is 1.23 V versus RHE, as shown schematically on the right.

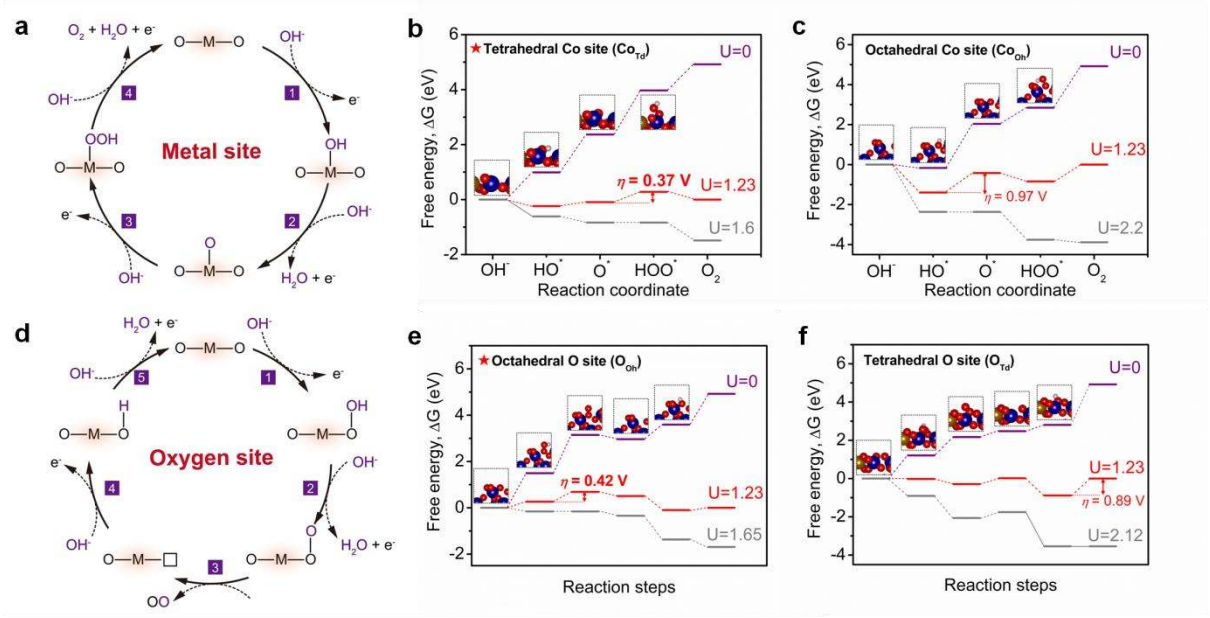

Figure 4. Identification of the active sites on hex-BSCF surface by DFT calculations. (a) Conventional OER mechanism on a metal ion site. The free energy under different potential U for OER on a Co ion at (b) a tetrahedral and (c) an octahedral site. (d) Lattice-oxygen participation mechanism, where □ represents an oxygen vacancy. The free energy under different potential U for OER on an oxygen ion at (e) an octahedral and (f) a tetrahedral site. The insets are as-built surface structure models of hex-BSCF with adsorbates.

A new complex oxide with unique hexagonal structure consisting of one ordered $(Co/Fe)O_{15}$ cluster, $Ba_4Sr_4(Co_{0.8}Fe_{0.2})_4O_{15}$ (hex-BSCF)**,** is reported to show ultrahigh OER electrocatalytic activity because both the tetrahedral Co ions and the octahedral oxygen ions on the surface are active, as conformed by combined X-ray absorption spectroscopy analysis and theoretical calculations.

Keyword: complex oxide, coordination environment, dual active sites, honeycomb-like structure, oxygen evolution reaction

Yinlong Zhu, Hassan A. Tahini, Zhiwei Hu, Zhi-Gang Chen, Wei Zhou*, Alexander C. Komarek, Qian Lin, Hong-Ji Jin, Chien-Te Chen, Yijun Zhong, M. T. Fernández-Díaz, Sean C. Smith, Huanting Wang, Meilin Liu, Zongping Shao*

Boosting oxygen evolution reaction by creating both metal ion and lattice-oxygen active sites in a complex oxide

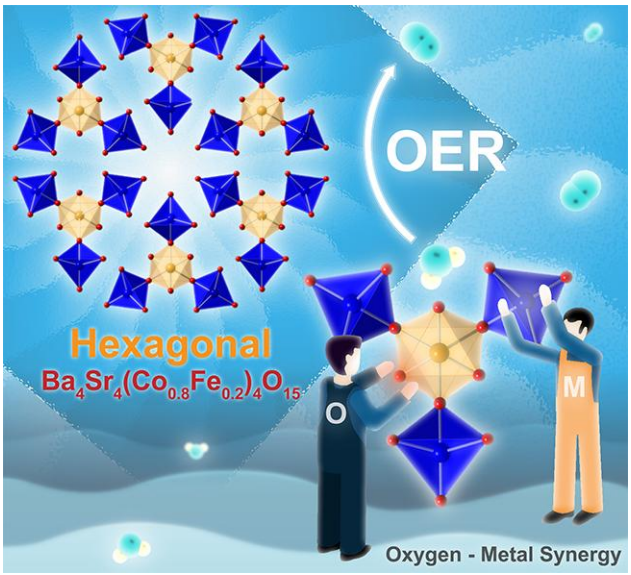

Supporting Information

Boosting oxygen evolution reaction by creating both metal ion and lattice-oxygen active sites in a complex oxide

Yinlong Zhu, Hassan A. Tahini, Zhiwei Hu, Zhi-Gang Chen, Wei Zhou, Alexander C. Komarek, Qian Lin, Hong-Ji Jin, Chien-Te Chen, Yijun Zhong, M. T. Fernández-Díaz, Sean C. Smith, Huanting Wang, Meilin Liu, Zongping Shao**

I. Experimental Section

Catalysts synthesis. Complex $Ba_4Sr_4(Co_{1-x}Fe_x)_4O_{15}$ ($0 \leq x \leq 1$) oxides and $Ba_{0.5}Sr_{0.5}Co_{0.8}Fe_{0.2}O_{3-\delta}$ (BSCF) perovskite used in this work were synthesized by a combined ethylenediaminetetraacetic acid-citric acid (EDTA-CA) complexing sol-gel method. Taking the synthesis of $Ba_4Sr_4(Co_{0.8}Fe_{0.2})_4O_{15}$ (hex-BSCF) as an example, Stoichiometric amounts of $Ba(NO_3)_2$, $Sr(NO_3)_2$, $Co(NO_3)_2 \cdot 6H_2O$ and $Fe(NO_3)_3 \cdot 9H_2O$ (both analytical grade, Sinopharm Chemical Reagent Co., Ltd.) were mixed in deionized water. EDTA and citric acid were then added as complexing agents in sequence at a mole ratio of 1:1:2 for total metal ions/EDTA/citric acid. To ensure complete complexation, the pH of the solution was adjusted to 6-7 by the addition of an NH_3 aqueous solution. A transparent gel was obtained by heating at 90 °C under stirring. The gel was then heated in the furnace at 250 °C for 5 h in air to form a solid precursor. Finally, the solid precursor was calcined at 1000 °C for 5 h in air to form hex-BSCF powder. The other materials (e.g., hex-BSC and BSCF) were also synthesized by the identical procedure as hex-BSC, with the exception of the distinction of their raw materials. The RuO_2 catalyst used in this study was purchased from Alfer Aesar.

Characterization. XRD patterns of the prepared powders were collected using an X-ray diffractometer (Rigaku Smartlab) equipped with filtered Cu-Kα radiation (λ = 1.5418 Å) by

step scanning with an interval of 0.02° in the 2θ range of 10-90°. Rietveld refinements of XRD were performed using the GSAS-EXPGUI package. NPD measurements were performed at the D2B diffractometer at the ILL in Grenoble, France. Rietveld refinements of NPD were performed using the FullProf program suite. SAED patterns and he corresponding HRTEM images were obtained using FEI Tecnai G2T20 operated at an accelerating voltage of 200 kV. SEM images were obtained using a Hitachi S-4800 scanning electron micro-analyzer. Nitrogen adsorption isotherms were tested under 77 K (BELSORP II) and the specific surface areas were calculated by the BET methods. Mössbauer spectroscopy of hex-BSCF was recorded using a conventional constant acceleration spectrometer (OXFORD-MS500) with a gray source of 25 mCi ^{57}Co in a palladium matrix moving at room temperature. The absorber was kept static in a temperature controllable cryostat. All isomer shifts are quoted relative to a-Fe at room temperature. The Mössbauer spectrum was fitted using the MOSSWINN 3.0 program. Soft XAS was performed at the 11A beam line of the NSRRC in Taiwan. The Co-$L_{2,3}$ and Fe-$L_{2,3}$ XAS spectra were obtained using the TEY mode, and the O-*K* XAS spectra were measured in both TEY mode and the bulk sensitive fluorescence-yield (FY) mode simultaneously. To calibrate the energy scale, NiO, CoO and Fe_2O_3 single crystals were measured simultaneously for the O-*K,* Co-$L_{2,3}$ and Fe-$L_{2,3}$ edges, respectively.

Electrode preparation. Working electrodes for OER tests were prepared by a controlled drop-casting method on a RDE (Pine Research Instrumentation, 5 mm diameter). The RDE was pre-polished with aqueous alumina suspension on a polishing cloth. To eliminate the electrode conductivity restriction within thin film working electrodes, the catalysts in this work were mixed with as-obtained conductive carbon (Super P Li) at a mass ration of 1:1. Briefly, a 5 μL aliquot of the catalyst ink, which was prepared by sonication of a mixture of 10 mg of oxide powder and 10 mg of conductive carbon dispersed in 1mL ethanol and 100 μL of 5 wt% Nafion solution for at least 1 h, was dropped on the electrode surface, generating an

approximate catalyst loading of 0.464 mg_{total} cm^{-2} (0.232 mg_{oxide} cm^{-2}) and was left to dry before the electrochemical tests.

Electrochemical measurements. OER performance in 0.1 M KOH solution was conducted using in a standard three-electrode electrochemical cell (Pine Research Instrumentation) with an RDE configuration controlled by a CHI 760D electrochemistry workstation. Catalysts cast on RDE, Pt foil and Ag|AgCl (3.5M KCl) were used as the working electrode, counter electrode, and reference electrode, respectively. During the measurement, RDE electrode was constantly rotating at 1600 rpm to get rid of the bubbles. The electrolyte was bubbled with O_2 for ~30 min prior to OER measurements and maintained under O_2 atmosphere throughout the test period. OER polarization curves were collected by capacitance-corrected cyclic voltammetry (CV) curves at a scan rate of 10 mV s^{-1} from 0.2 to 1 V vs. Ag|AgCl. Polarization curves were *iR* corrected in this work unless noted otherwise. The polarization curves were replotted as overpotential (η) versus the logarithm of current density (log |J|) to obtain Tafel plots. The chronopotentiometric test was conducted at a constant current density of 10 mA cm^{-2}. Cycle voltammetry (CV) method was used to measure the electrochemical double layer capacitance (C_{dl}). The potential was swept at different scan rates of 20, 40, 60, 80 and 100 mV s^{-1} from 0.2 to 0.25 V vs. Ag|AgCl where no faradic current was observed. The halves of the positive and negative current density differences at the center of the scanning potential range (i.e., 0.225 V for OER) were plotted versus scan rates where the slopes represent the double layer capacitance. The overall water splitting tests were performed in a two-electrode system with catalysts loaded on carbon paper (mass loading: 0.5 mg_{oxide} cm^{-2}).

Computational methods. Density functional theory calculations were performed using the Vienna *ab-initio* Simulation Package (VASP).[S1] Exchange and correlation were described using the generalised gradient approximation (GGA) with the Perdew-Burke-Ernzerhof (PBE) functional.[S2] Core and valence electrons were accounted for using the projector augmented

wavefunction (PAW) [S3] method and a cutoff energy of 500 eV. A Hubbard U_{eff} = 3.3 eV was applied on Co 3*d* electrons to account for correlation effects. Ba/Sr configurations in $Ba_4Sr_4Co_4O_{15}$ were modelled using the special quasirandom (SQS) technique,[S4] and the resulting bulk structures were fully relaxed using a $2 \times 2 \times 4$ Γ centered k-points mesh until forces and energies changed by no more than 0.01 eV/Å and 1×10^{-5} eV, respectively. Surfaces of hex-BSCF possess complex terminations. To effectively model the surface, we used an eight layer (0001) termination that exposes the three tetrahedral sites along with an octahedral site which is located about 0.7 Å below the surface. The (0001) surface of hex-BSCF was used in our theoretical investigation considering that it is among the most usually observed ones in the experimental TEM studies. Periodic images were separated by ~15 Å along the *z*-direction. OER mechanisms were modelled using the conventional mechanism following Nørskov et al.[S5,S6] using three intermediates, O^*, OH^* and OOH^*. Additional oxygen-lattice participation was accounted for by studying the adsorption on the O sites according to the recent work of Grimaud *et al*.[S7] The O 2*p* band center was calculated by taking the centroid of the projected DOS, including both occupied and unoccupied states, relative to the Fermi level.

II. Supplementary Results

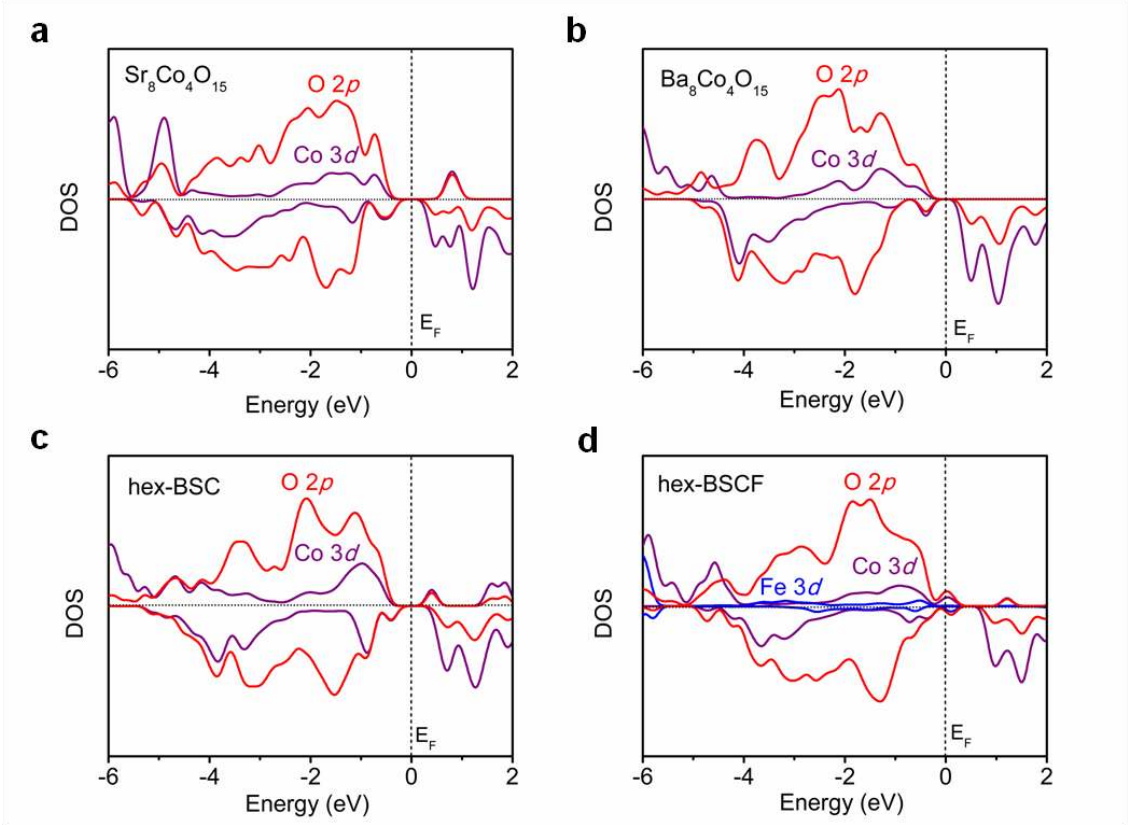

Figure S1. The partial density of states calculations of (a) $Sr_8Co_4O_{15}$, (b) $Ba_8Co_4O_{15}$, (c) hex-BSC and (d) hex-BSCF.

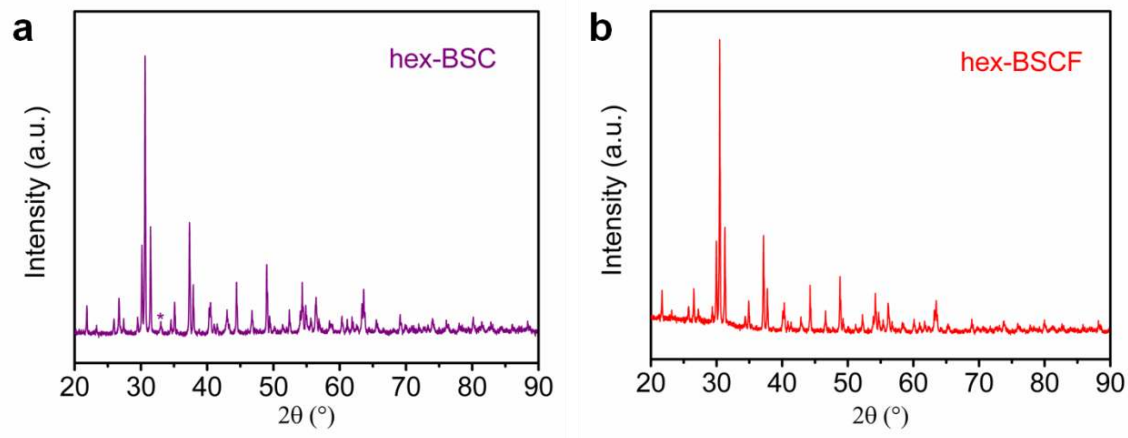

Figure S2. XRD patterns of (a) hex-BSC and (b) hex-BSCF. * indicates a tiny impurity peak in hex-BSC, but hex-BSCF has no observable impurity, implying the Fe substitution could stabilize the structure and promote the formation of pure phase.

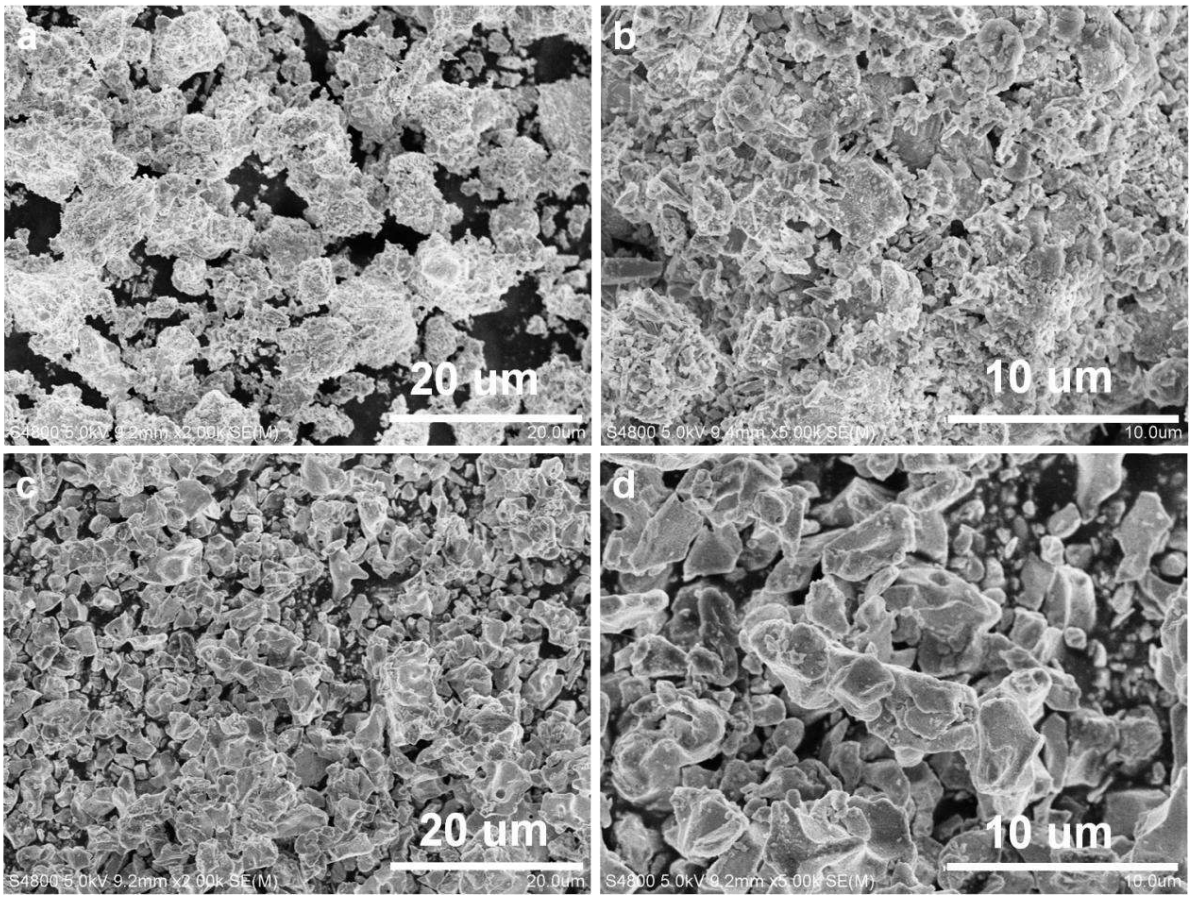

Figure S3. SEM images of (a, b) hex-BSC and (c, d) hex-BSCF with different magnifications.

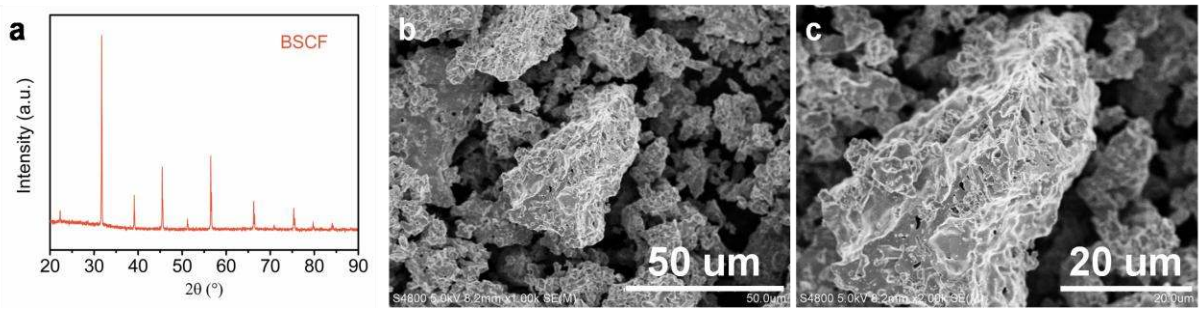

Figure S4. (a) XRD patterns of BSCF. (b, c) SEM images of BSCF with different magnifications.

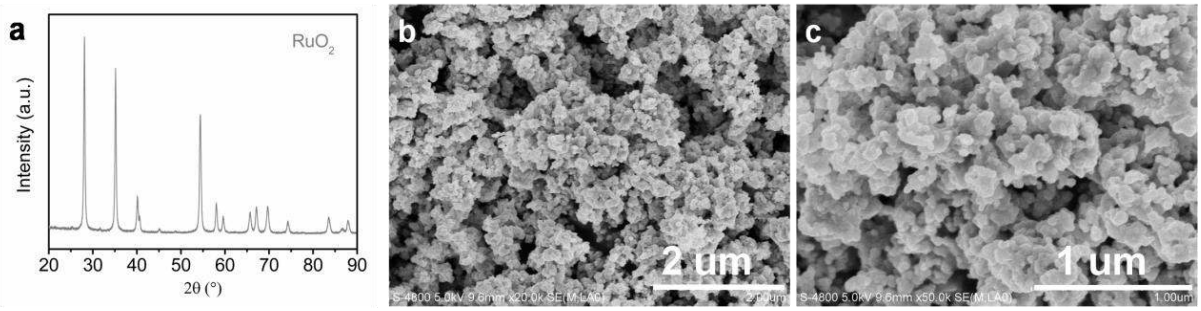

Figure S5. (a) XRD patterns of commercial RuO_2. (b, c) SEM images of commercial RuO_2 with different magnifications.

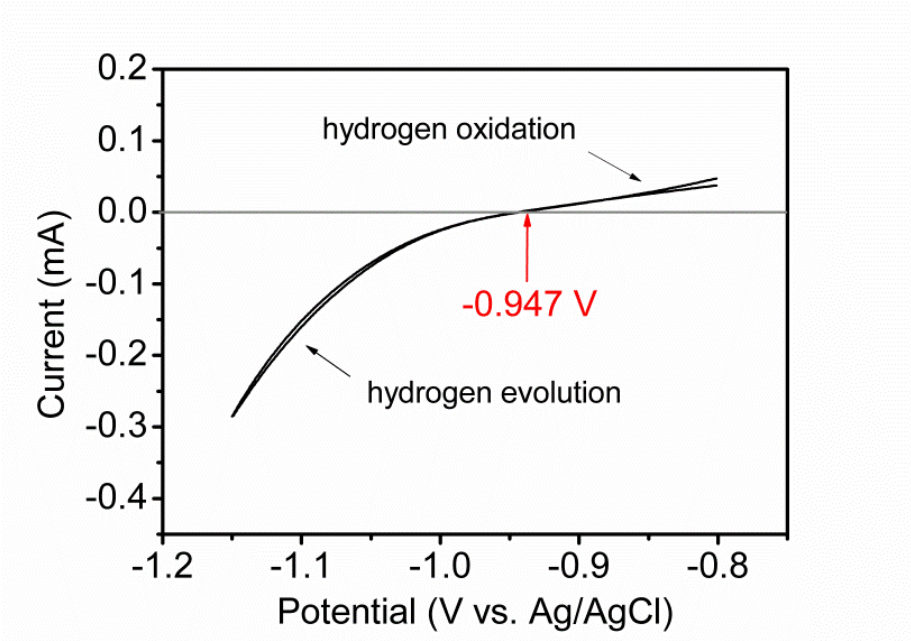

Figure S6. Potential calibration of the Ag/AgCl reference electrode in 0.1 M KOH solution. The calibration was performed in a high purity hydrogen-saturated electrolyte with a platinum rotating disk electrode (PINE, 4 mm diameter, 0.126 cm^2) as the working electrode. Cyclic voltammetry (CV) was run at a scan rate of 1 mV s^{-1}, and the average of the two potentials at which the current crossed zero was taken to be the thermodynamic potential for the hydrogen electrode reaction. In 0.1 M KOH, $E_{RHE} = E_{Ag/AgCl} + 0.947$ V.

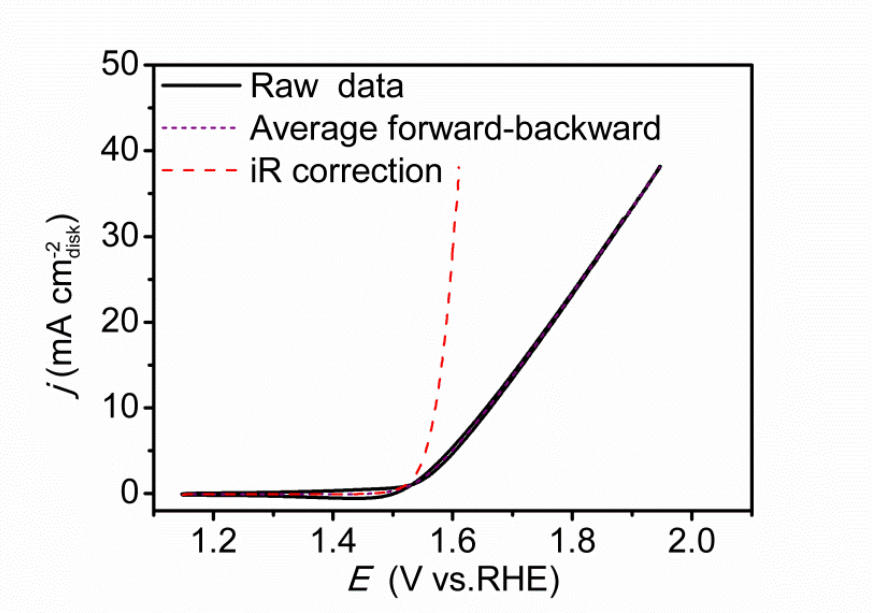

Figure S7. Capacitive and ohmic corrections of the as-measured CV curve (10 mV s^{-1}) of example catalyst (i.e., hex-BSCF).

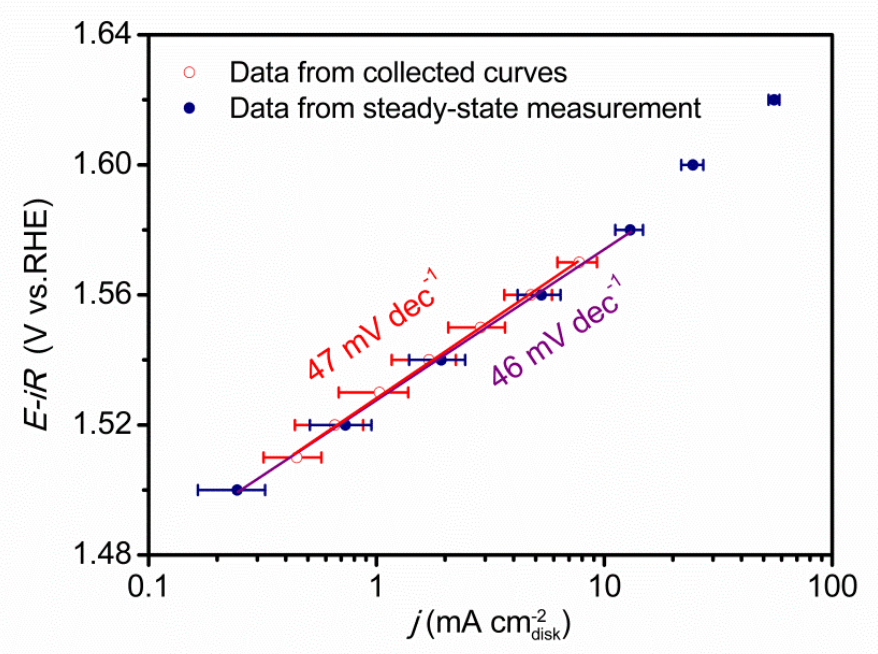

Figure S8. Comparison between Tafel plots (hollow circle) derived from the capacitance- and ohmic resistance-corrected OER activity curves as shown in Figure 2a and Tafel plots obtained from the steady-state measurements (solid square). Error bars represent standard deviations from three independent measurements. It can be seen that tafel plots (hollow circle) derived from the capacitance- and ohmic resistance-corrected OER activity curves are similar to the Tafel plots obtained from the steady-state measurements (solid circle). The use of steady-state measurement mainly removes the capacitive contribution to current. In the Tafel plots derived from the corrected CV curves (10 mV s^{-1}), the capacitive contribution is also properly removed (Figure S7). Thus, similar overpotentials are observed at the same current density for both methods.

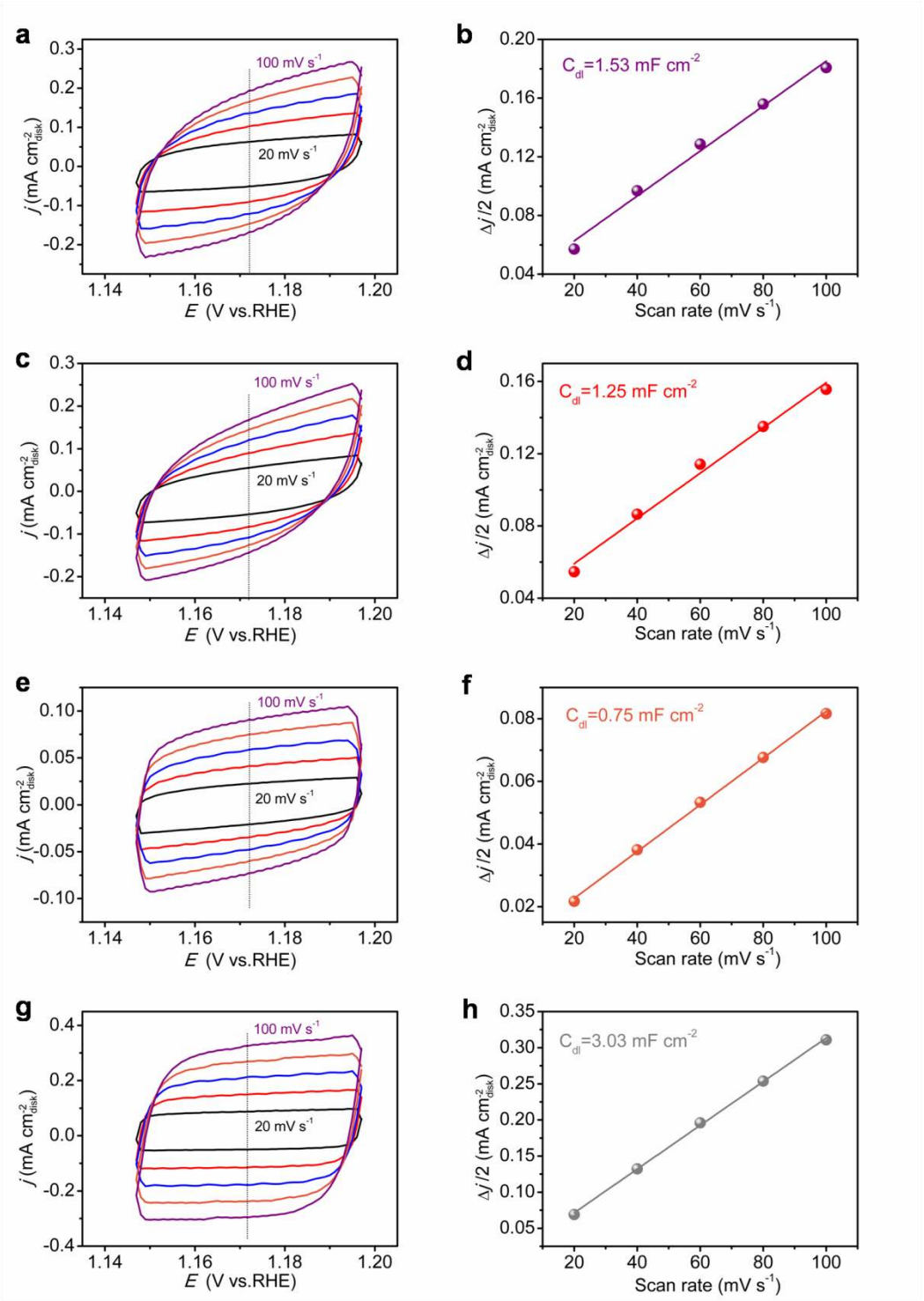

Figure S9. CV measurements in a non-faradic current region (1.147-1.197 V vs. RHE) at scan rates of 20, 40, 60, 80 and 100 mV s^{-1} of (a) hex-BSC, (c) hex-BSCF, (e) BSCF and (g) RuO_2 catalysts in 0.1 M KOH. Linear fitting of the capacitive currents versus CV scan rates for (b) hex-BSC, (d) hex-BSCF, (f) BSCF and (h) RuO_2 catalysts. The double-layer capacitance (C_{dl}) obtained from the CV method is expected to be linearly proportional to electrochemical surface area (ECSA).[S8-S10]

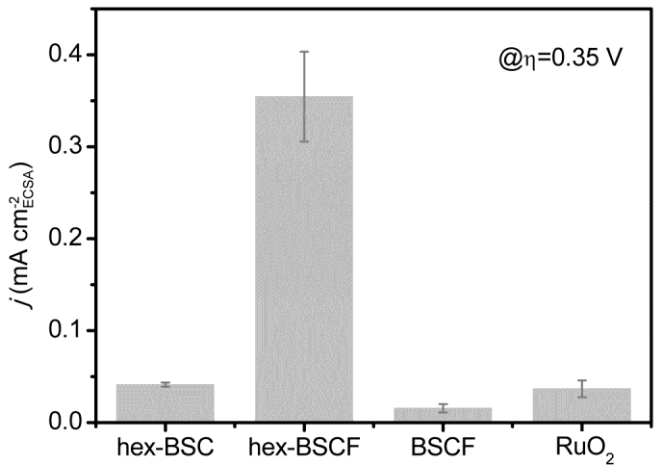

Figure S10. Specific activity normalized to ECSA of hex-BSC, hex-BSCF, BSCF and RuO_2 catalysts at η =0.35 V. The error bars represent standard deviations from at least three independent measurements.

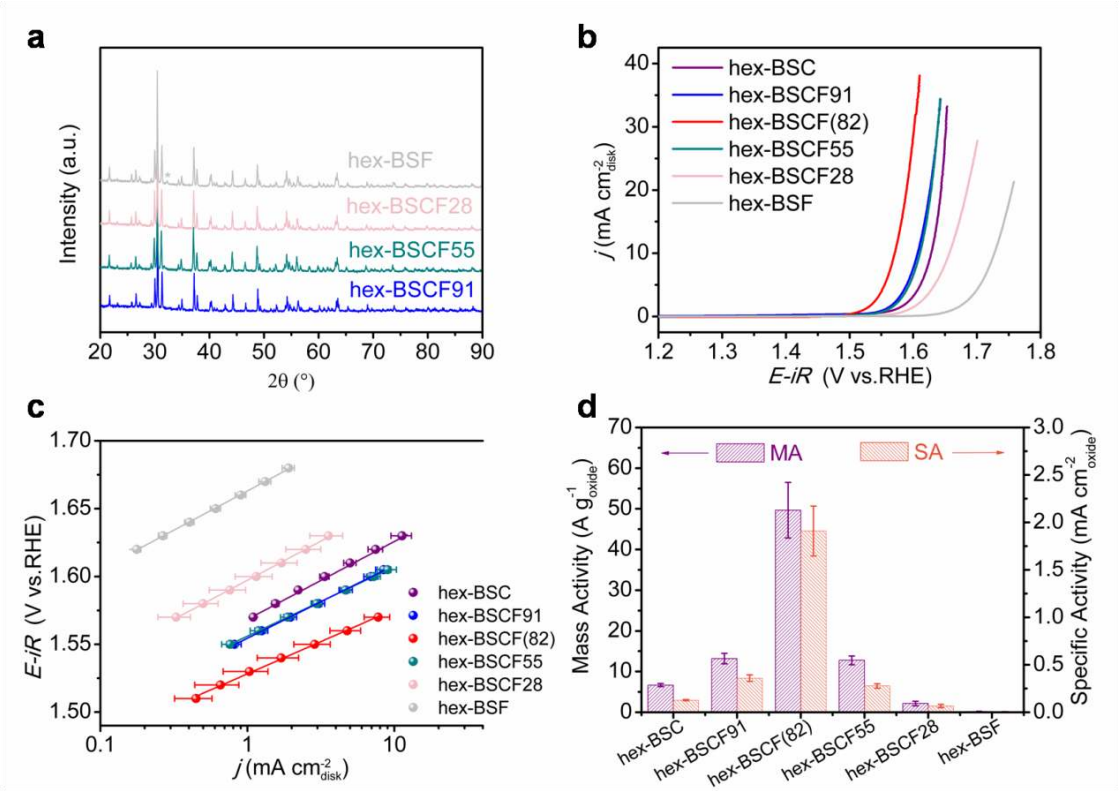

Figure S11. (a) XRD patterns of $Ba_4Sr_4(Co_{0.9}Fe_{0.1})_4O_{15}$ (denoted as hex-BSCF91), $Ba_4Sr_4(Co_{0.9}Fe_{0.1})_4O_{15}$ (denoted as hex-BSCF55), $Ba_4Sr_4(Co_{0.2}Fe_{0.8})_4O_{15}$ (denoted as hex-BSCF28) and $Ba_4Sr_4Fe_4O_{15}$ (denoted as hex-BSF). * indicates a tiny impurity peak in hex-BSF. (b) Capacitance- and ohmic resistance-corrected polarization curves of $Ba_4Sr_4(Co_{1-x}Fe_x)_4O_{15}$ (x=0, 0.1, 0.2, 0.5, 0.8, 1) catalysts in O_2-saturated 0.1 M KOH solution. (c) Corresponding Tafel plots. (d) Mass activities and BET surface area-normalized specific activities of $Ba_4Sr_4(Co_{1-x}Fe_x)_4O_{15}$ (x=0, 0.1, 0.2, 0.5, 0.8, 1) catalysts at η = 0.35 V.

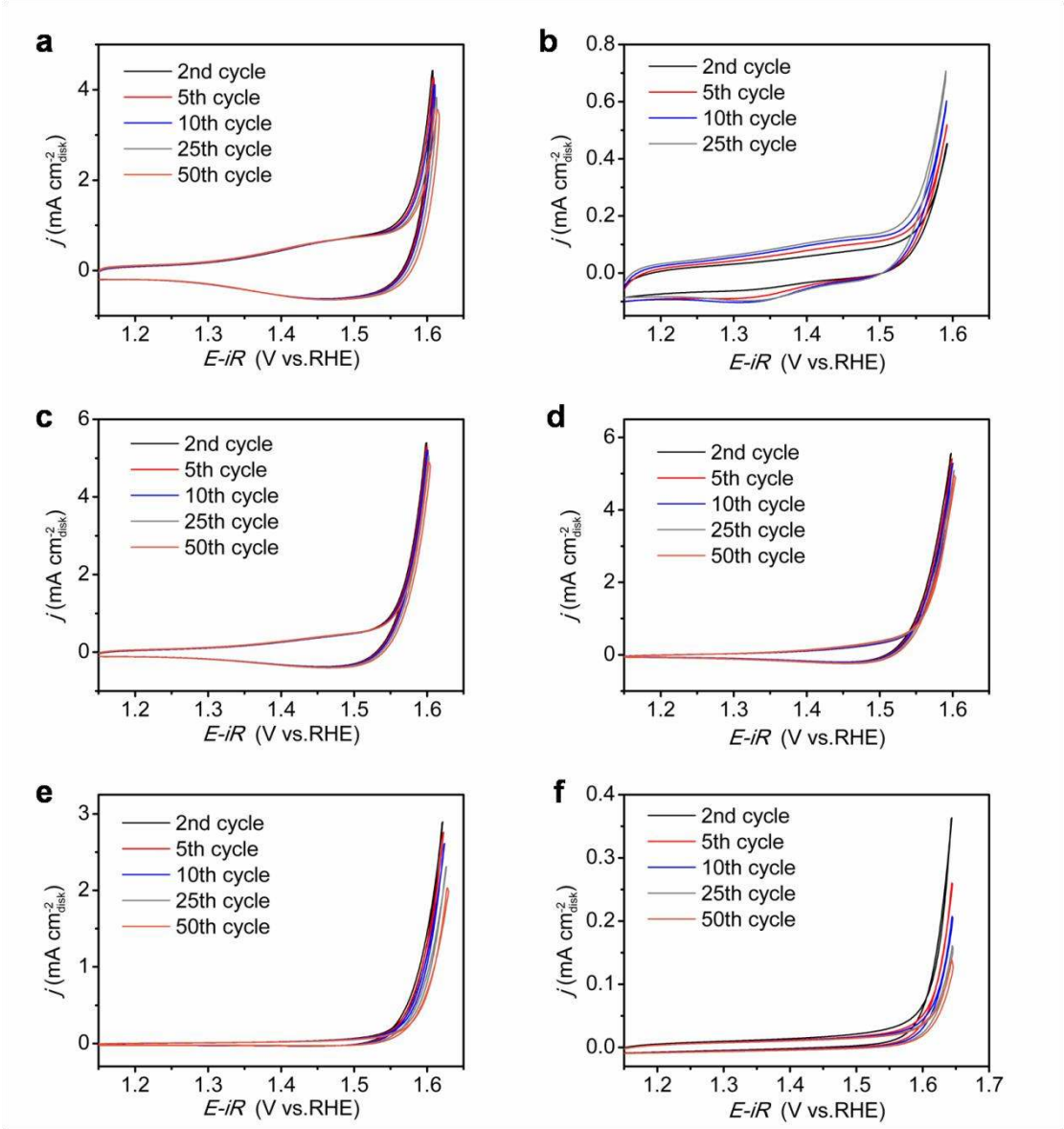

Figure S12. The 2nd, 5th,10th, 25th and 50th CV scans of (a) hex-BSC, (b) BSCF, (c) hex-BSCF91, (d) hex-BSCF55, (e) hex-BSCF28 and (f) hex-BSF.

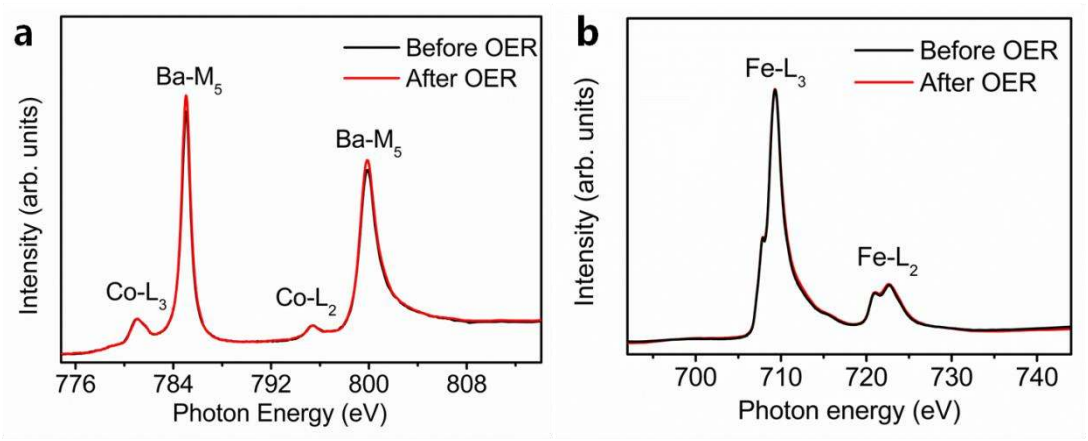

Figure S13. Soft (a) Co-$L_{2,3}$ and (b) Fe-$L_{2,3}$ XAS spectra of hex-BSCF before and after OER (i.e., 50 CV cycles). The Co-$L_{2,3}$ and Fe-$L_{2,3}$ XAS spectra of hex-BSCF before and after OER nearly completely overlap, indicative of no electronic structure variation (including oxidation state and spin state) on the surface of hex-BSCF under OER. The unchanged electronic structure therefore excludes the possibility of surface structure change during OER.

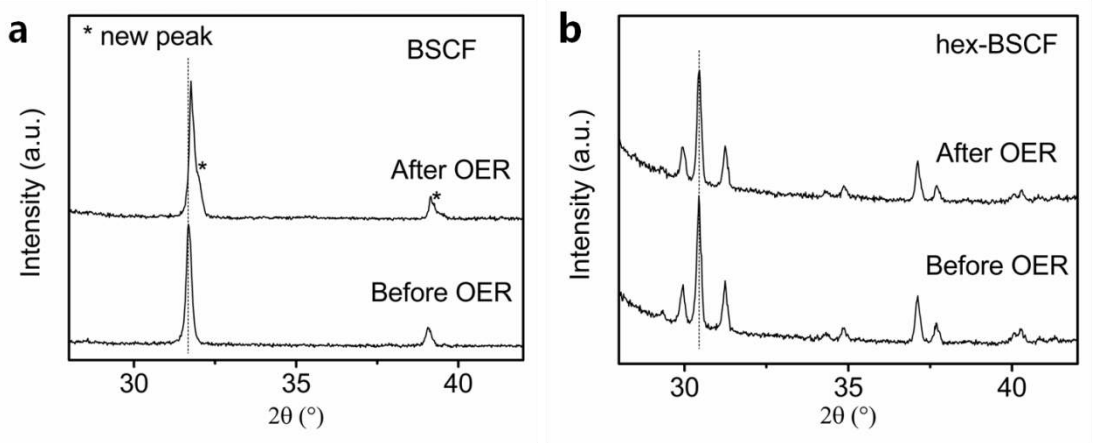

Figure S14. XRD patterns of (a) BSCF and (b) hex-BSCF before and after OER (i.e., 50 CV cycles). The XRD patterns show that there is no apparent variation in the peak pattern and position of hex-BSCF before and after OER, confirming that the crystal structure of hex-BSCF did not change during OER. In contrast, the main peaks of BSCF shifted to high degrees and new peaks appeared after OER, indicating the destruction of crystal structure of BSCF during OER.

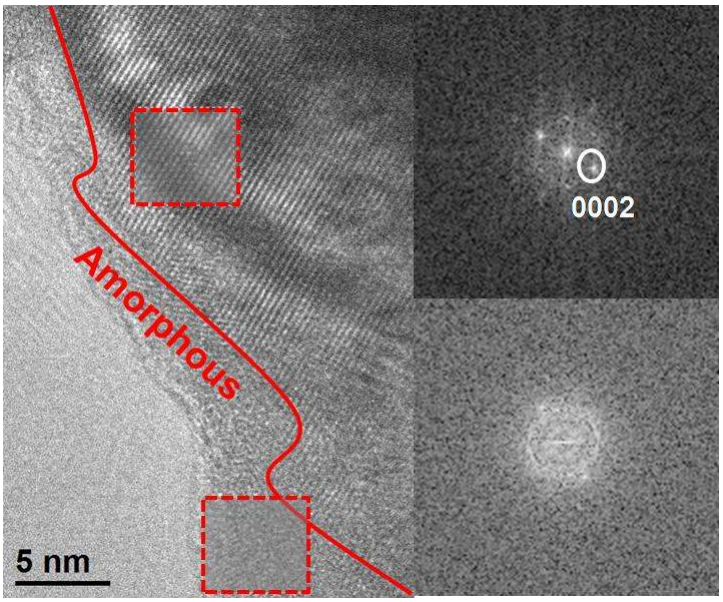

Figure S15. HRTEM image and the corresponding FFT patterns of the hex-BSC after 50-cycle CV scans

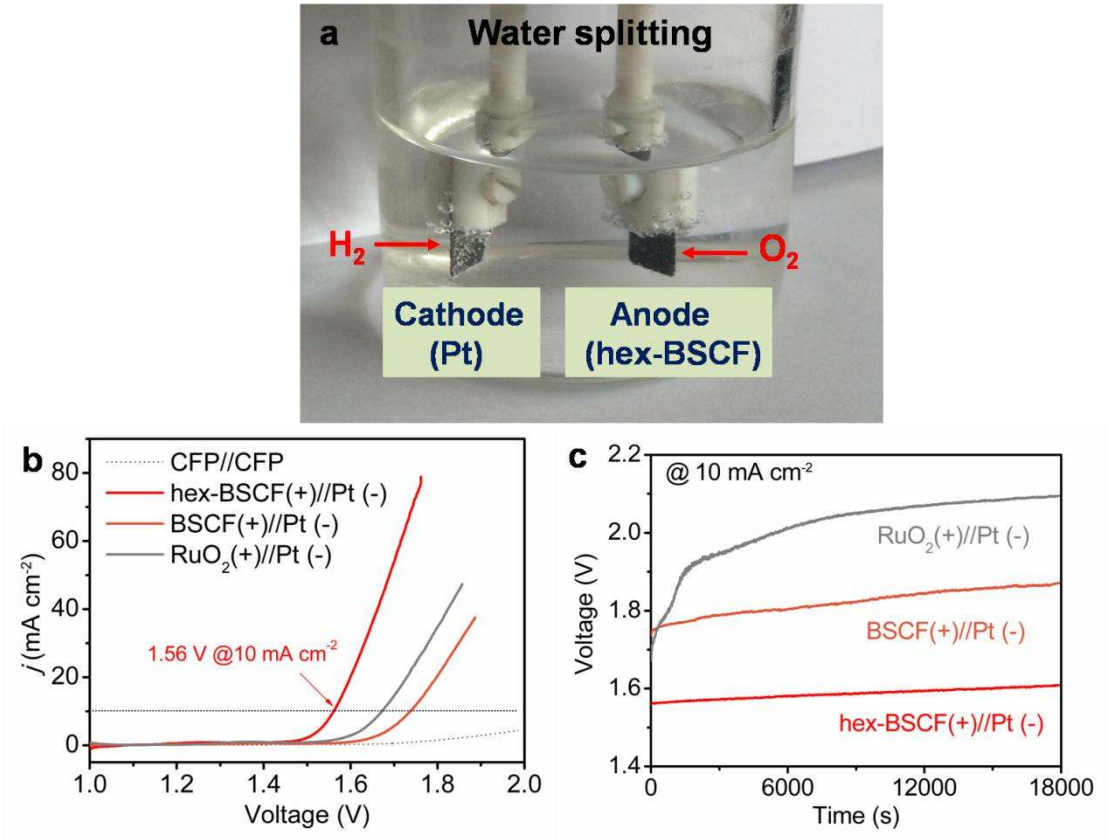

Figure S16. (a) A representative photograph of the two-electrode configuration using hex-BSCF as the anode and Pt as the cathode. (b) Polarization curves of bare CFP//CFP, hex-BSCF(+)//Pt(-), BSCF(+)//Pt(-) and RuO_2(+)//Pt(-) for overall water splitting in 1 M KOH solution. (c) Chronopotentiometric curve of water electrolysis at a constant current density of 10 mA cm^{-2}.

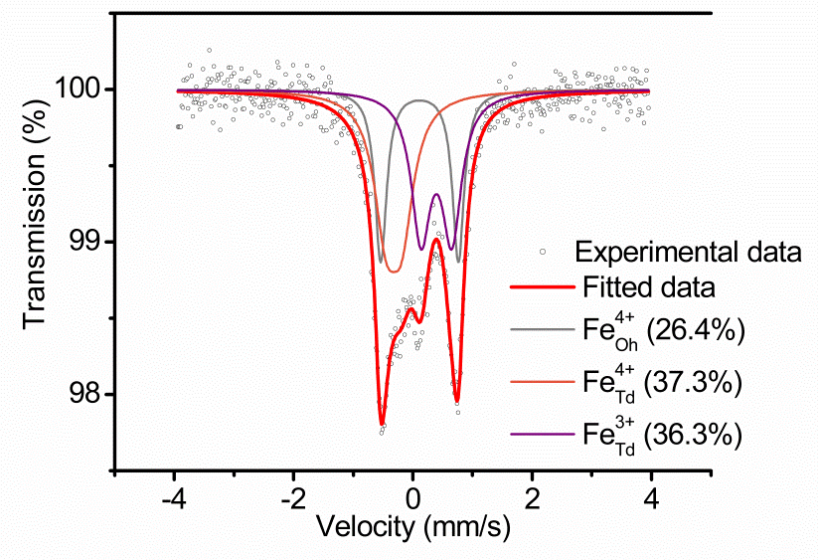

Figure S17. XPS Mössbauer spectra of hex-BSCF.

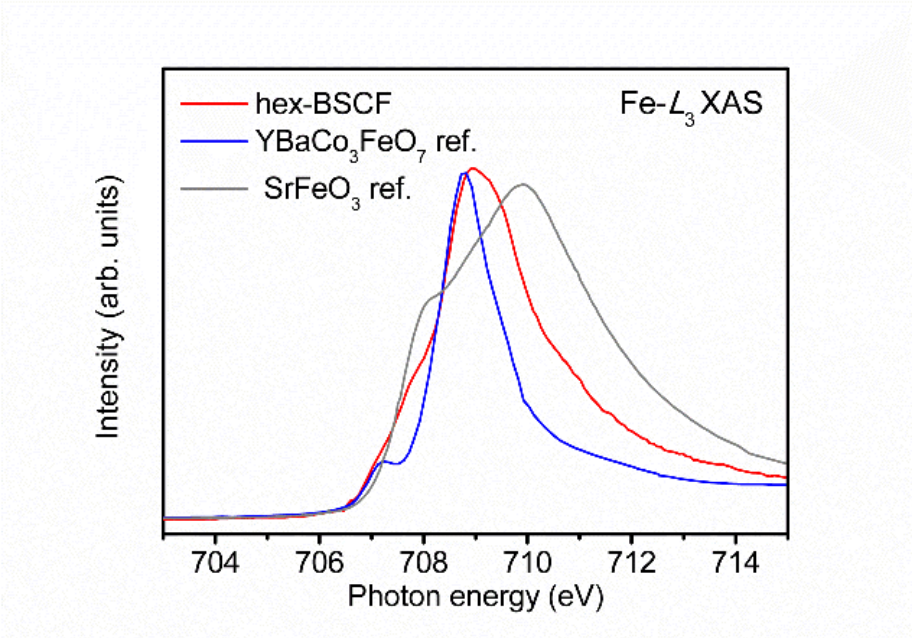

Figure S18. Fe L_3-edge XAS spectra of hex-BSCF and reference materials (HS Fe^{3+}_{Td} for $YBaCo_3FeO_7$; HS Fe^{4+}_{Oh} for $SrFeO_3$).

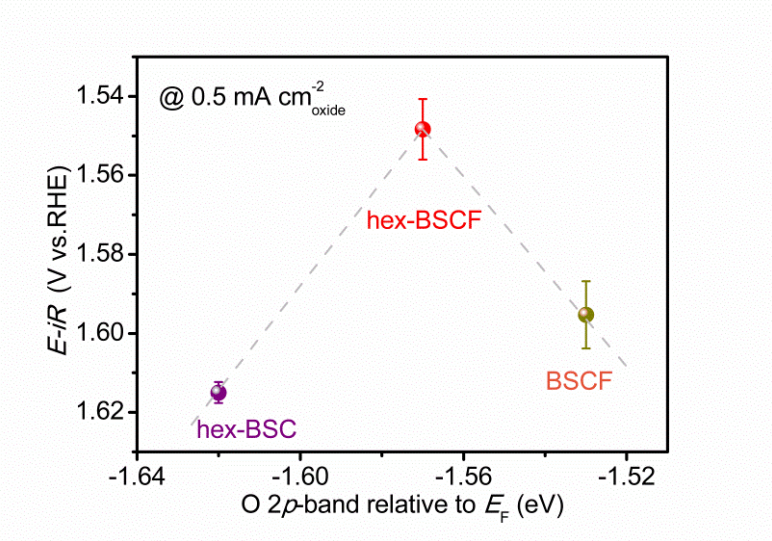

Figure S19. Evolution of the *iR*-corrected potential at 0.5 mA cm^{-2}_{oxide} versus the O 2*p*-band centre relative to E_F (eV) of hex-BSC, hex-BSCFand BSCF. The error bars represent standard deviations from at least three independent measurements.

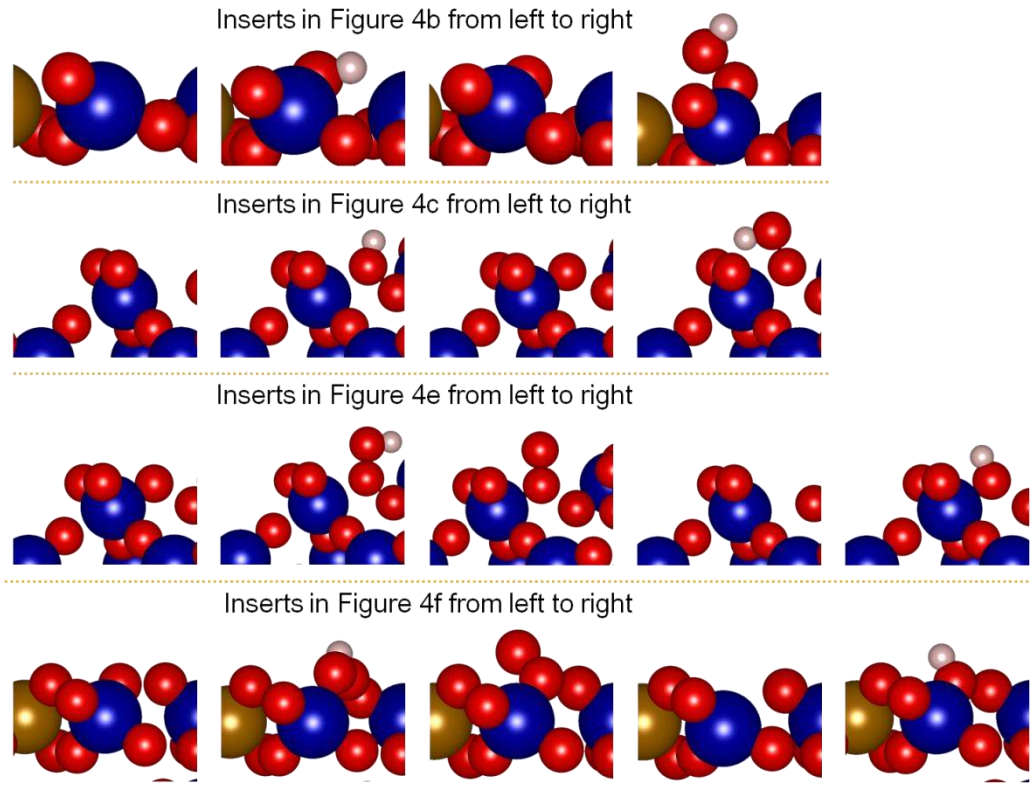

Figure S20. As-built surface structure models of hex-BSCF with adsorbates in Figure 4.

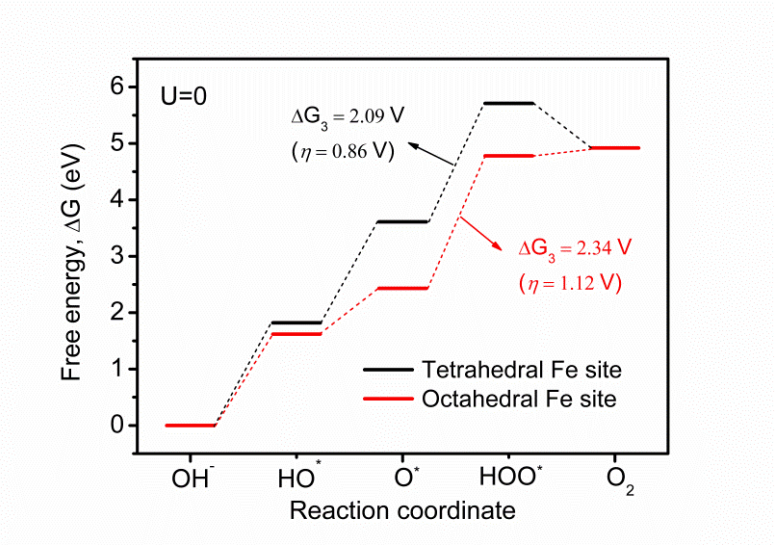

Figure S21. The OER free energy diagrams of hex-BSCF on the tetrahedral and octahedral Fe sites.

Table S1. Refined structural parameters of hex-BSCF from NPD data.

Atom	Wyckoff position	S.O.F	x	y	z	Beq
Sr1	2*a*	1	0	0	-0.0358	0.0087(4)
Ba1	2*b*	1	0.33333	0.66667	0.4576(12)	0.0087(4)
Sr2	6*c*	1	0.47778(12)	0.52212(12)	0.7945(8)	0.0087(4)
Ba2	6*c*	1	0.17364(19)	0.82626(19)	0.1336(9)	0.0087(4)
Co1	2*b*	0.74(1)	0.33333	0.66667	-0.0186(14)	0.0018(8)
Fe1	2*b*	0.26(1)	0.33333	0.66667	-0.0186(14)	0.0018(8)
Co2	6*c*	0.86(1)	0.1762(2)	0.8237(2)	0.6345(11)	0.0018(8)
Fe2	6*c*	0.14(1)	0.1762(2)	0.8237(2)	0.6345(11)	0.0018(8)
O1	12*d*	1.00(1)	0.6789(2)	0.0668(2)	-0.0078(7)	0.0135(3)
O2	6*c*	1.00(1)	0.25082(18)	0.74907(18)	0.8058(10)	0.0135(3)
O3	6*c*	1.00(1)	0.41020(17)	0.58970(17)	0.1312(9)	0.0135(3)
O4	6*c*	1.00(1)	0.90646(16)	0.09344(16)	0.2330(9)	0.0135(3)

$P6_3mc$, a = 11.60263(16) Å, c = 6.84595(13) Å, R_p=1.71%, R_{wp}=2.24%, and χ^2= 8.37.

Refined composition: $Ba_4Sr_4(Co_{0.827}Fe_{0.173})_4O_{15.0(1)}$

Table S2. BET specific surface areas of the catalysts.

Samples	Specific surface area $A_{s(BET)}$ /m^2 g^{-1}
hex-BSC	5.25
hex-BSCF (hex-BSCF82)	2.60
hex-BSCF91	3.61
hex-BSCF55	4.61
hex-BSCF28	3.24
hex-BSF	2.68
BSCF	0.37
RuO_2	10.2

Table S3. Comparison of OER activity for hex-BSCF with reported state-of-the-art oxide-based electrocatalysts supported on glass carbon electrode in 0.1 M KOH, including simple oxides, spinel oxides, Li-containing oxides, perovskite oxides, perovskite hydroxides and complex oxides, etc.

Catalysts	Mass loading (mg cm^{-2})	η @10 mA cm^{-2} (mV)	Tafel slope (mV dec^{-1})	Specific activity @η=0.35 V (mA cm^{-2}_{BET})	References
hex-BSCF	**0.232**	**340**	**47**	~2	**This work**
$Pr_{0.5}Ba_{0.5}CoO_{3-\delta}$	0.25	~400	~60	~2	*Nat. Commun.* **2013**, *4*, 2439
LT-$Li0.5CoO_2$	0.25	~390	60	N.A.	*Nat. Commun.*, **2014**, *5*, 3949
$CaCu_3Fe_4O_{12}$	0.25	~370	51	~1.5	*Nat. Commun.* **2015**, *6*, 8249
Co_3O_4@CoO nanocube[a]	0.025	430	89	N.A.	*Nat. Commun.*, **2015**, *6*, 8106
80nm $LaCoO_3$	0.25	490	79	~0.02	*Nat. Commun.* **2016**, *7*, 11510
$PrBa_{0.5}Sr_{0.5}Co_{1.5}Fe_{0.5}O_{5+\delta}$ nanofiber	0.202	358	52	~0.18	*Nat. Commun.* **2017**, *8*, 14586
p-SnNiFe	0.25	350	35	N.A.	*Nat. Commun.* **2017**, *8*, 394
$La_{0.5}Sr_{1.5}Ni_{0.7}Fe_{0.3}O_{4.04}$	0.0153	360	44	~3	*Nat. Commun.* **2018**, *9*, 3150
$SrCoO_{2.7}$	0.0153	419	67	~4	*Nat. Commun.*, **2018**, *9*, 3150
$LaCo_{0.8}Fe_{0.2}O_3$ (oLCFO-Ar)[b]	1.07	350	59	N.A.	*Sci. Adv.* **2016**, *2*, e1600495
Amorphous $Ba_{0.5}Sr_{0.5}Co_{0.8}Fe_{0.2}O_{3-\delta}$[b]	0.0168	500	65	N.A.	*Sci. Adv.* **2017**, *3*, e1603206
$Nd_{1.5}Ba_{1.5}CoFeMnO_{9-\delta}$	0.209	359	81	~0.3	*Sci. Adv.* **2018**, *4*, eaap9360
$La_{0.5}Ba_{0.25}Sr_{0.25}CoO_{2.9-\delta}F_{0.1}$	0.157	~470	122	~0.3	*Chem* **2018**, *4*, 2902
α-MnO_2-SF	0.204	490	78	<0.02	*J. Am. Chem. Soc.* **2014**, *136*, 11452
$Ca_2Mn_2O_5$	0.255	>470	149	N.A	*J. Am. Chem. Soc.* **2014**, *136*, 14646
$BaN_{i0.83}O_{2.50}$	0.295	~420	N.A[c]	~2	*J. Am. Chem. Soc.* **2016**, *138*, 3541
La_2NiMnO_6-1[d]	N.A.	370	58	N.A.	*J. Am. Chem. Soc.* **2018**, *140*, 11165
$SrNb_{0.1}Co_{0.7}Fe_{0.2}O_{3-\delta}$	0.232	500	76	~1	*Angew. Chem. Int. Ed.* **2015**, *54*, 3897
O_2-treated BSCF	0.639	550	129	~0.4	*Adv. Mater.* **2015**, *27*, 266
$Ca_{0.9}Yb_{0.1}MnO_{2.65}$	N.A.	~470	68	N.A.	*Adv. Mater.* **2015**, *27*, 5989
$LiNi_{0.8}Al_{0.2}O_2$	0.051	~410	44	~2	*Adv. Mater.* **2015**, *27*, 6063
$LaMn_7O_{12}$	0.25	>570	98	~0.04	*Adv. Mater.* **2017**, *29*, 1603004
$Y_2[Ru_{2-x}Y_x]O_{7-y}$	0.637	~500	112	~0.06	*Nano Lett.* **2017**, *17*, 3974
Delithiated Li(Ni,Fe)PO_4	N.A.	425	52	N.A.	*Energy Environ. Sci.* **2015**, *8*, 1719
50 nm	0.639	~370	97	~0.2	*Energy Environ.*

$La_{0.7}(Ba_{0.5}Sr_{0.5})_{0.3}Co_{0.8}Fe_{0.2}O_{3-\delta}$					*Sci.* **2016**, *9*, 176
$Pb_2Ru_2O_{6.5}$	0.637	~410	114	N.A.	*Energy Environ. Sci.* **2017**, *10*, 129
$SrCo_{0.95}P_{0.05}O_{3-\delta}$	0.232	480	84	~0.02	*Adv. Funct. Mater.* **2016**, *26*, 5862
$SrNb_{0.1}Co_{0.7}Fe_{0.2}O_{3-\delta}$ nanorod	0.232	389	61	~0.03	*Adv. Energy Mater.* **2017**, *7*, 1602122
$CaMnO_3$/S-300	0.1	470	N.A.[c]	~0.05	*Adv. Energy Mater.* **2018**, *8*, 1800612
NiO-$(La_{0.613}Ca_{0.387})_2NiO_{3.562}$	0.36	373	42	~0.1	*Nano Energy* **2015**, *12*, 115
(A-PBCCF-H nanofiber)[e]	0.232	410	99	~0.06	*Nano Energy* **2017**, *32*, 247
$LaSr_3Co_{1.5}Fe_{1.5}O_{10-\delta}$	0.255	388	84	~0.15	*Nano Energy* **2017**, *40*, 115
$SrSc_{0.025}Nb_{0.025}Co_{0.95}O_{3-\delta}$	0.36	~380	~55	~10	*Mater. Horiz.* **2015**,*2*, 495
$BaCo_{0.7}Fe_{0.2}Sn_{0.1}O_{3-\delta}$	0.232	~420	69	~0.6	*Adv. Sci.* **2016**, *3*, 1500187

[a]: The electrolyte is 0.5 M KOH. [b]: The catalyst substrate is nickel foam.
[c]: N.A.=Not available. [d]: The electrolyte is 1 M KOH.
[e]: A-PBCCF-H =H_2-treated $(PrBa_{0.8}Ca_{0.2})_{0.95}(Co_{1.5}Fe_{0.5})_{0.95}C_{o0.05}O_{5+\delta}$.

Table S4. Fitted data of Mössbauer spectroscopy for hex-BSCF.

	δ (mm/s)	***Qs*** (mm/s)	FWHM (mm/s)	Area Ratio (%)
Fe^{4+}_{Oh}	0.17±0	1.3±0	0.12±0	26.4
Fe^{4+}_{Td}	-0.26±0	0.27±0.1	0.24±0	37.3
Fe^{3+}_{Td}	0.45±0	0.52±0	0.20±0	36.3

Supplementary References

[S1] G. Kresse, J. Furthmüller, *Phys. Rev. B* **1996**, *54*, 11169.

[S2] J. P. Perdew, K. Burke, M. Ernzerhof, *Phys. Rev. Lett*. **1996**, **77**, 3865.

[S3] P. E. Blöchl, *Phys. Rev. B* **1994**, *50*, 17953.

[S4] A. van de Walle, P. Tiwary, M. de Jong, D. L. Olmsted, M. Asta, A. Dick, D. Shin, Y. Wang, L. -Q. Chen, Z. -K. Liu, *Calphad* **2013**, *42*, 13.

[S5] I. C. Man, H. Y. Su, F. Calle-Vallejo, H. A. Hansen, J. I. Martínez, N. G. Inoglu, J. Kitchin, T. F. Jaramillo, J. K. Nørskov, J. Rossmeisi, *ChemCatChem* **2011**, *3*, 1159.

[S6] J. Rossmeisl, Z. W. Qu, H. Zhu, G. J. Kroes, J. K. Nørskov, *J. Electroanal. Chem.* **2017**, *607*, 83.

[S7] A. Grimaud, O. Diaz-Morales, B. Han, W. T. Hong, Y. L. Lee, L. Giordano, K. A. Stoerzinger, M. T. M. Koper, Y. Shao-Horn, *Nat. Chem.* **2017**, *9*, 457.

[S8] Y. Zhu, W. Zhou, Y. Zhong, Y. Bu, X. Chen, Q. Zhong, M. Liu, Z. Shao. *Adv. Energy Mater.* **2017**, *7*, 1602122.

[S9] X. Xu, Y. Chen, W. Zhou, Z. Zhu, C. Su, M. Liu, Z. Shao, *Adv. Mater.* **2016**, *28*, 6442.

[S10] C. C. McCrory, S. Jung, J. C. Peters, T. F. Jaramillo, *J. Am. Chem. Soc.* **2013**, *135*, 16977.